

# Scientific Imagers as High-Energy Radiation Sensors

*Doctoral Thesis Proposal*

May 23, 2017  
Revised, July 10, 2017

*Author:*  
Ashley CARLTON

*Thesis Advisor:*  
Prof. Kerri CAHOY

*Thesis Committee:*  
Prof. Daniel HASTINGS  
Dr. Insoo JUN  
Prof. Harlan SPENCE

Space, Telecommunications, Astronomy, and Radiation (STAR) Laboratory  
Department of Aeronautics and Astronautics  
Massachusetts Institute of Technology



# *Abstract*

## **Scientific Imagers as High-Energy Radiation Sensors**

by Ashley CARLTON

Harsh radiation in the form of ionized, highly energetic particles is part of the space environment and can affect spacecraft. These particles not only sweep through the solar system in the solar wind and flares and ejected from galactic and extra-galactic supernovae, but are also trapped as belts in planetary magnetic fields. Spacecraft operating in radiation environments can experience component failures, degradation of sensors and solar panels, and serious physical damage to materials.

The Jovian magnetosphere is the largest and strongest of the planets in the solar system. Measuring and characterizing charged particles are fundamental to understanding the energetic processes powering the magnetosphere, interactions with the satellites of Jupiter, and the effects on spacecraft near or in Jovian orbit. High-energy megaelectron volt (MeV) electrons can penetrate through atmospheres of rocky bodies, such as Jupiter's moon, Europa, physically and chemically weathering the surfaces of the satellites, affecting albedo and surface chemistry.

Measurements of the high-energy ( $>1$  MeV) electron environment at Jupiter are currently spatially and temporally limited. For the most part, the information about the Jovian environment comes from the Galileo spacecraft Energetic Particle Detector (EPD) (in Jovian orbit from December 1995 to September 2003), which had a nearly equatorial orbit. Juno, a NASA spacecraft that entered Jovian orbit in July 2016, and Europa Clipper, a NASA mission planned for the 2020s, do not carry instruments capable of measuring  $>1$  MeV electrons due to resource limitations (cost, size, schedule, complexity). Juno is in a polar orbit and Europa Clipper is planned to be in a highly elliptical Jovian orbit, flying-by Jupiter's moon, Europa, in every orbit.

It is desirable to develop ways to use existing hardware on spacecraft to describe the environment. Solid-state detectors are used as scientific imagers on spacecraft. In addition to being sensitive to incoming photons, semiconductor devices can also generate charge from incoming charged particles collected during integration and detector readout. These radiation hits from the environment are typically considered "noise" on the detector.

In this thesis, we develop a technique to extract quantitative high-energy electron environment information (energy and flux) from the radiation noise on science imagers. We use data from the Galileo spacecraft Solid-State Imaging (SSI) instrument, which is a silicon charge-coupled device (CCD). We process the flight data, extract radiation noise, and build histograms of the energy deposition on the detector by pixel. We simulate electron transport in the SSI using Geant4 to determine the energies of the source particles that can reach the detector (in the form of pixels with hits), the amount of energy that is deposited in the pixels, and the flux at a given energy.

To demonstrate that the general technique is applicable to other imagers, we will analyze the Galileo Near-Infrared Mapping Spectrometer (NIMS). To build confidence in the simulation modeling, we will also perform in-lab mono-energetic electron beam testing of a semiconductor device. This thesis will also include a summary of required and recommended information (tests, models, etc.) for the use of science imagers as high-energy electron sensors.



# Contents

<b>Abstract</b>	<b>iii</b>
<b>1 Introduction</b>	<b>1</b>
1.1 Background	1
1.2 Project Definition and Thesis Overview	1
1.3 Motivation for Characterizing the Jovian Radiation Environment	2
1.3.1 Science Motivation	2
1.3.2 Engineering Motivation	2
1.4 Motivation for Developing a Technique Using Science Imaging Instruments	3
<b>2 Literature Review</b>	<b>7</b>
2.1 Radiation in Solid-State Detectors	7
2.2 Science Imagers as Radiation Sensors	7
<b>3 Approach and Methodology</b>	<b>9</b>
3.1 Galileo Solid-State Imaging (SSI) Experiment	9
3.1.1 Experiment: Flight Data	10
3.1.2 Simulations	12
Preliminary Results - Energy	15
Preliminary Results - Flux Measurement	17
3.1.3 Example: SSI Observation 5101r, Orbit 22	17
3.2 Galileo Near Infrared Imaging Spectrometer (NIMS)	18
3.3 Validation	19
3.3.1 Galileo Energetic Particle Detector	19
3.3.2 In-Lab Testing	21
3.4 Descope Options	22
<b>4 Expected Contributions</b>	<b>23</b>
<b>5 Status and Proposed Schedule</b>	<b>25</b>
5.1 Classes and Degree Milestones	25
5.2 Research Schedule	26
<b>Bibliography</b>	<b>29</b>



# List of Figures

1.1	Map of the paths of spacecraft that have made high-energy measurements of the Jovian Magnetosphere. The Pioneer 10 and 11 flybys are plotted in green. The Voyager 1 and 2 flybys are in red. The Galileo orbits are in blue. Figure from <i>M. de Soria-Santacruz Pich et al., 2016</i> . . . . .	4
1.2	Graphic showing the energy ranges covered by instruments on spacecraft to Jupiter. The shaded regions correspond to the energy ranges of concern for specific radiation effects. The blue shaded region covers the radiation dose and dose rate risks. The red region covers the internal charging and internal electrostatic discharge (IESD) risks. The green shaded region covers the surface charge risk. The Pioneers and Voyagers spacecraft made high-energy electron measurements in the zones of concern, but those missions were only flybys, resulting in a limited temporal and spatial measurement. Galileo Energetic Particle Detector (EPD) made measurements over a period of 35 orbits, mainly equatorially around Jupiter. Juno orbits over the polar region of Jupiter, but has limited high-energy detection capabilities with respect to the risk of radiation dose and dose rate effects and damage. For the Europa Clipper mission, currently in development, there are no dedicated high-energy particle measurements planned. . . . .	5
1.3	Orbit plans for Juno and Europa Clipper on the left and right, respectively. Original images are from [31] and [22] and they have been annotated for clarity. Note, the Juno orbit has been updated since Jupiter Orbit Insertion (JOI). . . . .	6
3.1	Approach to extracting high-energy information from the SSI flight data. . . . .	10
3.2	Diagram of the Galileo spacecraft with the main components and instruments labeled. The SSI is part of the scan platform, to the bottom right of the drawing, labeled in red. The EPD is to the top right of the drawing, labeled in blue. Image source: NASA, 1989, <a href="https://solarsystem.nasa.gov/galleries/galileo-diagram-labeled">https://solarsystem.nasa.gov/galleries/galileo-diagram-labeled</a> . . . . .	11
3.3	Digital number (DN) to energy deposited conversion for the SSI gain states. . . . .	12
3.5	Removing the target (moon, Europa) from the image. (a) Digital number (DN) as a function of distance from the center of the moon. The vertical line is drawn at 95 pixels from the center of the moon, dividing the moon from the dark sky. (b) Image with the moon subtracted, leaving on the dark sky with radiation hits. . . . .	12
3.4	SSI image of Europa from 2002-01-18 15:16:32.0 in orbit 33. The image was taken as a subset of the 800 x 800 array. The exposure duration is 195.83 ms and the readout is 8.667 s. The gain mode is 100K, or 377.4 e-/DN. The image was taken at 17.7 $R_J$ (L-shell of 17.0). The intensity scale is in digital number (DN). . . . .	13
3.6	Histogram of the energy deposited in the moon-removed image. The lower x-axis is the digital number and the upper x-axis labels the corresponding energy deposited in keV. . . . .	14

3.7	Cut-away visualization of the geometry built in Geant4 of the SSI. The key components are labeled. The colors correspond to the material of the element (yellow - silicon, dark blue - aluminum, cyan - titanium, green - invar, pink - silica, red orange - tantalum, brown - printed wiring board). . . . .	14
3.8	Histograms of the energy deposited from the Geant4 simulations of 5, 10, 30, 50, 100, and 200 MeV electrons. We set the histogram bin widths to 1 keV. . .	15
3.9	Energy deposited in the detector (left y-axis) as a function of the energy of the particle at the detector for 100 MeV electrons. The primary particles are red circles and the secondaries are blue circles. The collision stopping power is plotted in green on the right y-axis. . . . .	16
3.10	Photograph (left) and labeled diagram (right) of the NIMS instrument from <i>Carlson et al., 2012</i> . The telescope is on the right, the radiative cooler is facing left and the spectrometer is behind. . . . .	19
3.11	Galileo EPD >11 MeV integral flux channel (DC3) as a function of distance from Jupiter in $R_J$ . . . . .	20
3.12	Galileo EPD >11 MeV integral flux channel as a function of distance from Jupiter in $R_J$ . The results from five SSI images analyzed to date are plotted on top of the EPD measurements. The error bars for each SSI image are within the size of the data point. . . . .	21

# List of Tables

1.1	Spacecraft that have made high-energy (>1 MeV) electron measurements at Jupiter. . . . .	3
1.2	Overview of Jovian radiation models. . . . .	4
3.1	Gain state for converting digital number to electrons. The gain state ratio factors are found in the calibration files. Uncertainties from the original calibration can be found in the JPL calibration report [35]. Temperatures are in Kelvin (K). . . . .	10
3.2	Results of Geant4 simulations for particles that reach the SSI detector and deposit energy. The Geant4 simulations are of $1e9$ electrons with energies 1, 3, 5, 10, 30, 50, 100, and 200 MeV. Columns B and C are the numbers of unique primary and secondary particles that deposit energy on the detector, respectively, and their sum is in Column D. Column E is the total number of pixels with energy deposition ("hits") and Column G is the ratio of particle hits to pixel hits (Column D divided by Column E). Column F is the percentage of the 800 by 800 pixel array that has hits. . . . .	16
3.3	Geometric scale factor $G_2$ that relates the particle count rate at the detector to the environmental flux for a given energy. . . . .	18
5.1	This table shows my coursework to date as well as the expected course this fall. I am on track to meet all academic doctoral requirements. . . . .	25
5.2	This table shows my degree milestones to date and anticipated milestones. Dates in italics are tentative. I am on track to meet all degree requirements. . . . .	25



## Chapter 1

# Introduction

### 1.1 Background

High-energy charged particles are trapped in planetary magnetospheres, the region of space surrounding an astronomical object in which charged particles are controlled by that object's magnetic field, and can affect spacecraft and satellites orbiting the planet. Jupiter's magnetosphere is the largest and strongest of a planet in the solar system. The bow shock extends about  $84 R_J$  towards the Sun (where  $R_J = 71,492$  km is the radius of Jupiter), and the magnetotail can extend almost as far in the other direction as Saturn's orbit ( $\sim 50$ - $1000 R_J$ , or up to  $\sim 71$  million km) [34, 38]. Similar to Earth, Jupiter is roughly a magnetic dipole with a tilt of  $\sim 11^\circ$  [21, 34]. Jupiter's magnetic field strength is an order of magnitude larger than Earth, and its magnetic moment is roughly 18,000 times larger [47]. The Jupiter magnetosphere is powered by a liquid dynamo circulating metallic hydrogen. Eruptions of sulfur and oxygen from the moon Io's volcanoes form a cold torus that rotates with Jupiter, generating ions through collisions and UV radiation, altering the dynamics of and supplying the mass to the magnetosphere [30, 33, 48]. The Jovian radiation environment is dominated by high-energy electrons, which can cause increased radiation dose damage and risk of internal electrostatic discharge [17]. The high-energy electron spectra extends to much higher energies than the spectra found at Earth [5, 43, 53].

### 1.2 Project Definition and Thesis Overview

A magnetosphere is described by its structure, composition, and dynamics. Determining the types and energies of the particles is critical to understanding the energetic processes powering the magnetosphere and for studying interactions with the satellites (and rings and upper atmosphere) of Jupiter. High-energy ( $>1$  MeV) electron environment measurements are sparse, both spatially and temporally. For the most part, the information about the Jovian environment comes from the Galileo spacecraft Energetic Particle Detector (EPD) [56]. Galileo was in Jovian orbit from December 1995 to September 2003 and orbited around the equator of Jupiter.

The Juno spacecraft, currently in orbit at Jupiter, and the Europa Clipper spacecraft, in Phase B of mission design with plans to orbit a moon of Jupiter, Europa, would contribute much needed spatial and temporal variability to the dataset. However, Juno and the plans for Europa Clipper do not include a high-energy ( $>1$  MeV electron) detection capability due to resource limitations (cost, size, schedule, complexity).

This thesis develops a technique to extract qualitative environment information (energy and flux) using existing hardware on spacecraft: solid-state devices, or "science imagers". We focus our study on scientific imagers for two reasons: (1) scientific imagers are common to exploration spacecraft, such as those designed for Jupiter, and (2) since radiation effects

are a well-observed and studied phenomena in imagers, there are well-documented techniques for extracting radiation "hits". Imagers, such as star trackers, could also use such a technique for Earth-orbiting satellites. We focus on electrons  $>1$  MeV since measurements of  $<1$  MeV electrons are possible with the Juno spacecraft and science imagers are likely more shielded, preventing lower energies from reaching the detector.

We develop the technique using data from the Galileo spacecraft Solid-State Imaging (SSI) instrument, which is a charge-coupled device (CCD). The radiation noise in the flight data is compared to charged particle transport simulations from Geant4. The results are then compared to the Galileo Energetic Particle Detector (EPD) for validation.

## 1.3 Motivation for Characterizing the Jovian Radiation Environment

### 1.3.1 Science Motivation

Knowledge of the high-energy radiation environment is important for our scientific understanding of the composition, structure, and dynamics of the magnetosphere. Increased temporal coverage and spatial measurements can improve current environment models.

High-energy electrons affect the Jovian satellites. The energetic electrons are a major contributor to exogenic processes which affect the albedo and surface chemistry of the moon [44]. MeV electrons can penetrate through the atmospheres of rocky bodies, physically and chemically weathering the surfaces of satellites. The penetration depths depend on the particle type, particle energy, and material, with particle doses at depths up to a few microns in rocky surfaces dominated by ions and at depths greater than  $10 \mu\text{m}$  by electrons [28, 29, 42]. The electrons are 10s of keV to  $>25$  MeV.

High-energy electrons can drive surface chemistry by ionization that catalyze chemical reactions, which has direct impacts on the astrobiological potential of a satellite. Since metabolic reactions within living cells depend on chemical energy, it has been suggested that the Europa subsurface ocean has a high potential for sustaining biological activity if some oxidation-reduction chemistry is present [10, 25]. It is highly likely that Europa's briny subsurface ocean is a reducing environment, and the irradiation of a surface by bombardment of charged particles leads to oxidation of the surface [11, 40].

### 1.3.2 Engineering Motivation

Knowledge of the high-energy radiation environment benefits spacecraft mission design, operations, and lifetime. For mission operations, radiation may limit observation modes in higher flux and higher energy regions. For example, on the Galileo spacecraft, during the nominal mission, the Solid-State Imaging (SSI) instrument only opened its shutter when the spacecraft was greater than approximately  $9 R_J$  from Jupiter. Mission architectures are affected by the estimated radiation environment, often trading mission lifetime against more desirable science that requires orbits with higher radiation exposure. The SSI was only operated at closer distances to Jupiter during the extended mission, up to  $5.8 R_J$  during Io flybys. The Europa Clipper mission flower-petal orbit is specifically designed to maximize science and mission life but minimizing radiation exposure during the orbit [46].

The risk of anomalies and degradation to spacecraft are increased in high-energy particle environments (*e.g.*, [3, 16, 26]). Single event effects occur due to high-energy particles ( $>10$  MeV protons and heavier ions) penetrating spacecraft shielding and striking electronic devices. Internal (or bulk) charging occurs when MeV electrons penetrate satellite shielding materials and deposit charge on internal spacecraft components. If the component's resistivity is high, the rate of charge build up can overcome the leakage rate property of the

material. The induced electric field may then exceed the breakdown threshold for the material, causing electrostatic discharge (ESD) in the material [3, 15, 17, 57]. Total ionizing dose (TID) is a result of long-term radiation absorption and can lead to undesirable effects such as electron-hole pair production, transport, and trapping in the dielectric material. The total accumulated dose depends on orbit parameters (altitude, inclination, eccentricity), spacecraft orientation, and time. The integrated particle energy spectrum (fluence as a function of particle energy) is used to compute the TID. As TID increases, material and component degradation increases, leading to reduced functionality and greater susceptibility to failure. There is also evidence that dose rate affects the TID; electron-hole pair production, transport, and trapping in dielectrics can be more pronounced at lower dose rates (“enhanced low dose rate sensitivity,” ELDRS) (see *Chen et al.* (2010) and references therein [9]).

Increased information about the environment can supplement and refine models of the environment [14, 53] that are used for spacecraft design. The survivability and lifetime estimates are developed based on the anticipated environment, influencing part selection (radiation tolerant or not), redundancy, shielding design (thickness, material, location), and software development (scrubbing, self-inspection, or not).

## 1.4 Motivation for Developing a Technique Using Science Imaging Instruments

High-energy particle information about the Jovian magnetosphere is limited, both spatially and temporally. Table 1.1 shows a list of the spacecraft that have taken high-energy particle measurements. We limit the list to instruments capable of measuring electrons because it is the focus of this thesis. Figure 1.1 shows a plot of the orbit paths of the satellites that have recorded high-energy particle measurements with respect to Jupiter. The Pioneers 10 and 11 and Voyagers 1 and 2 made measurements during flybys in the 1970s and 1980s, respectively. For the most part, the information about the Jovian environment comes from the Galileo spacecraft Energetic Particle Detector (EPD) [56] (in Jovian orbit from December 1995 to September 2003). While there were 35 orbits from 5  $R_J$  to over 100  $R_J$ , the latitude is only approximately  $\pm 10^\circ$  from the equator<sup>1</sup>.

TABLE 1.1: Spacecraft that have made high-energy (>1 MeV) electron measurements at Jupiter.

Spacecraft	Instruments	Measurements
Pioneer 10 (flyby, Dec. 1973), Pioneer 11 (flyby, Dec. 1974)	Geiger tube telescope (GTT) Trapped radiation detector (TRD) Electron current detector (ECD)	electrons >0.06, 0.55, 5, 21, 31 MeV electrons >0.16, 0.26, 0.46, 5, 8, 12, 35 MeV electrons >3.4 MeV
Voyager 1 (flyby, March 1979), Voyager 2 (flyby, 1979)	Cosmic ray telescope (CRT)	electrons 3-110 MeV
Galileo (35 orbits, Dec. 1995 – Sept. 2003)	Energetic particle detector (EPD)	electrons 0.238, 0.416, 0.706, 1.5, 2.0, and 11.0 MeV

The first comprehensive model of the Jovian environment and the standard for decades was the Divine and Garrett model in 1983, which is built on empirical data from the Pioneers and Voyagers spacecraft [14]. The D&G model was updated in 2005 to include synchrotron measurements from Earth-based observatories [18]. Presently, there are two models that are used as the standard. The Jovian Specification Environment (JOSE) model [51] by ONERA<sup>2</sup> in France, which is based on the Salammbô theoretical code [50] in combination with data from the Galileo EPD. The Galileo Interim Radiation Electron model version-2 (GIRE2)

<sup>1</sup>For reference, the average orbital radii for the Galilean moons are: Io: 5.9  $R_J$ , Europa: 9.4  $R_J$ , Ganymede: 15.0  $R_J$ , and Callisto: 26.3  $R_J$ .

<sup>2</sup>ONERA is the Office National d’Etudes et de Recherches Aérospatiales, which is the French national aerospace research center.

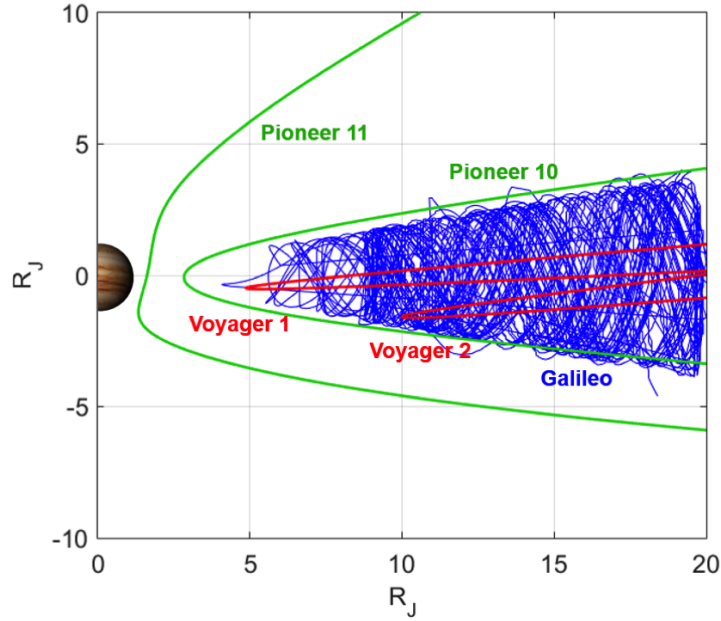


FIGURE 1.1: Map of the paths of spacecraft that have made high-energy measurements of the Jovian Magnetosphere. The Pioneer 10 and 11 flybys are plotted in green. The Voyager 1 and 2 flybys are in red. The Galileo orbits are in blue. Figure from *M. de Soria-Santacruz Pich et al., 2016*.

combines the Galileo EPD dataset with the original Divine and Garrett model (good coverage at  $R_J < 8$  from the Pioneer and Voyager spacecraft) and synchrotron observations to estimate the trapped electron radiation environment [54]. GIRE2 addresses discontinuities at the boundary between the GIRE and D&G model and extends the model from  $\sim 16 R_J$  (GIRE) up to  $\sim 50 R_J$  [19, 20]. Table 1.2 provides an overview of the models.

TABLE 1.2: Overview of Jovian radiation models.

Model Name	References	Description and Comments
Divine and Garrett (D&G)	Divine and Garrett, 1983	First comprehensive model of the radiation and plasma environment around Jupiter, Empirical, from Geiger tube telescope (GTT) on Pioneer 10 and 11, and from the cosmic ray telescope on Voyager 1 and 2.
Divine and Garrett (D&G), updated	Garrett et al., 2005	Included data from Earth-based observations of the Jupiter synchrotron emissions
Jovian Specific Environment (JOSE)	ONERA, France, Sicard-Piet et al., 2011	Based on Salammbô theoretical code in combination with data from the Energetic Particle Detector (EPD) on the Galileo spacecraft
Galileo Interim Radiation Electron (GIRE) and GIRE2	Garrett et al., 2002; Garrett et al., 2012; de Soria-Santacruz et al., 2016	Empirical model, uses 10-min averages from the EPD on Galileo, V2 addresses discontinuities at the boundary between GIRE and the D&G models and extends from $\sim 16 R_J$ to up to $\sim 50 R_J$

Juno, a NASA spacecraft that entered Jupiter orbit in July 2016, measures Jupiter's composition, gravity field, magnetic field, and polar magnetosphere. Nominal science operations started in December 2016. The science phase (altered from the original plan due to a issue with propulsion system) will consist of approximately 11 orbits before the nominal end of mission in February 2018. The Juno spacecraft orbits over the poles ( $90 \pm 10^\circ$  inclination) with a highly elliptical orbit, lasting approximately 53.5 days. The elongated orbit means that apojove reaches a distance of around 8 million kilometers, passing through

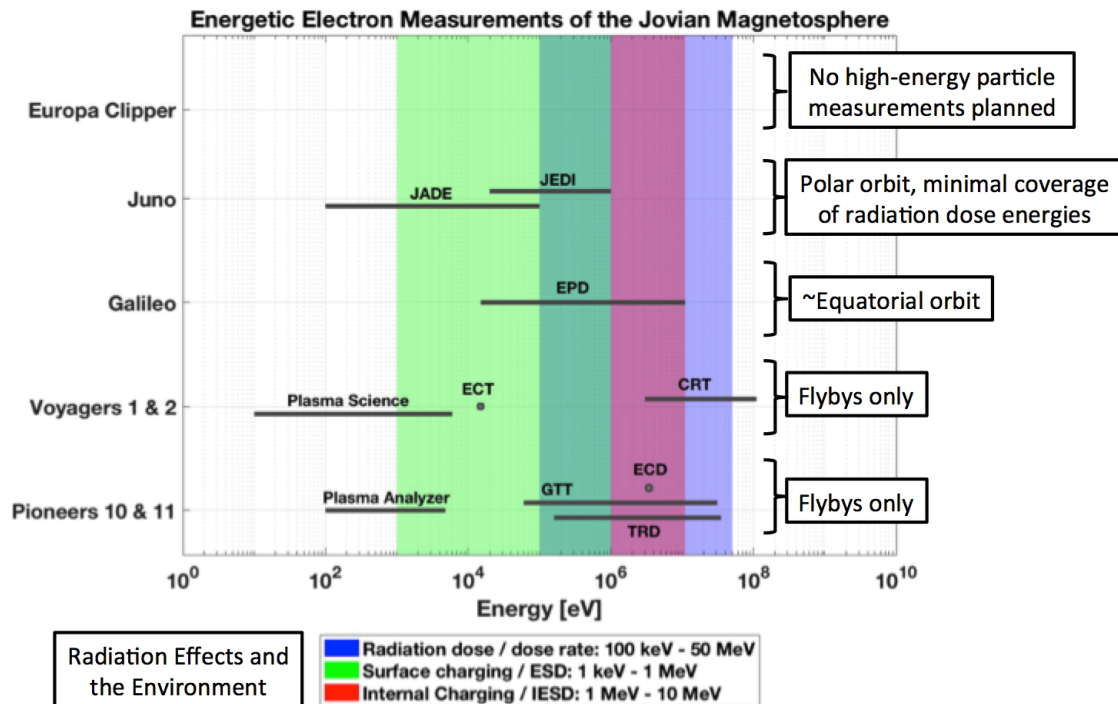


FIGURE 1.2: Graphic showing the energy ranges covered by instruments on spacecraft to Jupiter. The shaded regions correspond to the energy ranges of concern for specific radiation effects. The blue shaded region covers the radiation dose and dose rate risks. The red region covers the internal charging and internal electrostatic discharge (IESD) risks. The green shaded region covers the surface charge risk. The Pioneers and Voyagers spacecraft made high-energy electron measurements in the zones of concern, but those missions were only flybys, resulting in a limited temporal and spatial measurement. Galileo Energetic Particle Detector (EPD) made measurements over a period of 35 orbits, mainly equatorially around Jupiter. Juno orbits over the polar region of Jupiter, but has limited high-energy detection capabilities with respect to the risk of radiation dose and dose rate effects and damage. For the Europa Clipper mission, currently in development, there are no dedicated high-energy particle measurements planned.

Jupiter's magnetotail. Figure 1.3 shows the tilt of Juno's orbit relative to Jupiter and the radiation belts as the orbit shifts due to period reduction maneuvers. At perijove, the closest approach ranges from 4,200 km to 7,900 km.

Measurements of the high-energy electron environment from a polar orbiter would greatly increase the spatial data coverage. Juno is equipped with detectors with a maximum of 1 MeV for electrons and 3 MeV for protons. While this covers dose calculations and the primary science objectives, they do not cover higher energies, namely those of concern (radiation dose, single event effects, internal electrostatic discharges) of up to 30 MeV electrons and 100 MeV protons. See Figure 1.2 for the energy detection ranges for Juno's Jovian Auroral Distribution Experiment (JADE) and the Jupiter Energetic-particle Detector Instrument (JEDI) compared to the energy ranges of concern for radiation-related effects.

Juno has an orbit that, if higher energy (>1 MeV) particle measurements were taken, would significantly improve the spatial and temporal knowledge of the Jovian magnetosphere. A technique to extract high-energy electron information from science imagers already on Juno could yield important radiation environment information that would otherwise be unreported. Juno has three instruments that are CCDs: Juno Color Camera (Juno-CAM), the Advanced Stellar Compass (ASC), and the Stellar Reference Unit (SRU). Juno also has an Ultraviolet Spectrometer (UVS) that has a micro-channel plate. Each of these instruments presents an opportunity to extract environment information if there were a technique

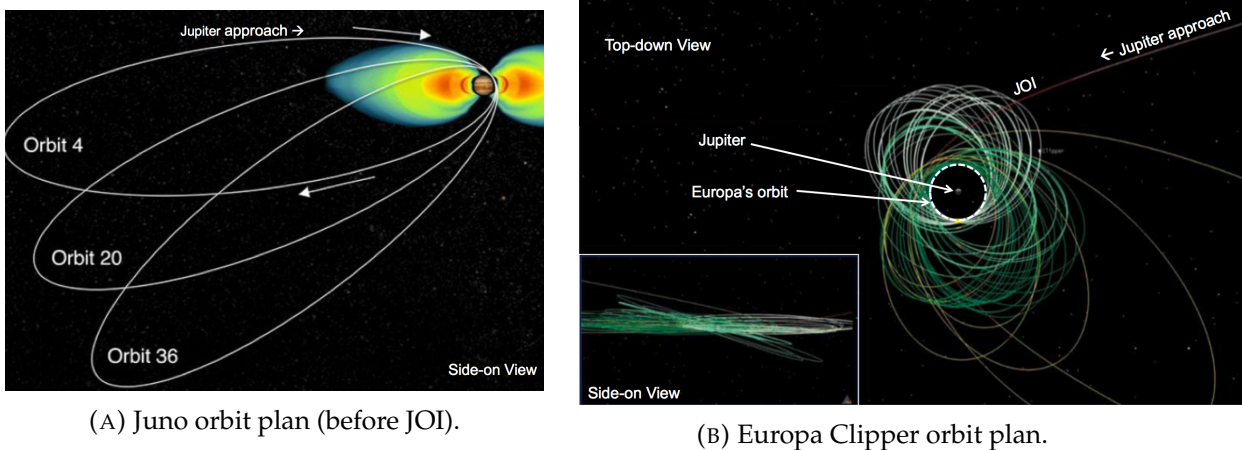


FIGURE 1.3: Orbit plans for Juno and Europa Clipper on the left and right, respectively. Original images are from [31] and [22] and they have been annotated for clarity. Note, the Juno orbit has been updated since Jupiter Orbit Insertion (JOI).

to do so.

Europa Clipper, currently in Phase B of design, is a NASA spacecraft designed to assess the habitability of Jupiter's icy moon, Europa. Europa Clipper will orbit Jupiter rather than Europa directly to avoid the high-radiation environment close to Jupiter (see Figure 1.3). On closest approach, Europa Clipper will come within 25 to 100 km of the surface of Europa. There are about 45 flybys of Europa planned for the 3.5-year mission. Mission lifetime will be limited by radiation [46].

At the time of writing, there are no instruments on Europa Clipper dedicated to MeV particle detection. However, there are instruments that are sensitive to MeV radiation: the Ultraviolet Spectrograph (UVS), Mapping Imager Spectrometer for Europa (MISE), Europa Imaging System (EIS), and MAss SPectrometer for Planetary EXploration (MASPEX). Since these instruments are sensitive to MeV radiation, they could be yield information about the high-energy radiation environment.

## Chapter 2

# Literature Review

### 2.1 Radiation in Solid-State Detectors

A solid-state detector is a photosensitive device that converts incoming photons into electric charge. The detecting medium is a semiconductor material such as a silicon or germanium crystal. Solid-state detectors include three main types of devices in astronomical imaging: charge-coupled devices (CCDs), complementary metal–oxide–semiconductors (CMOS), and infrared focal plane arrays (IRFPAs). Charge generation takes place at the silicon body of the device: when a photon interacts with silicon, it creates free electrons by a physical process known as the photoelectric effect, by promoting electrons into the conduction band. The generated electric current is converted to a digital signal when the device is read out [27].

A charged particle passing through the semiconductor material, such as silicon, creates electron-hole (e-h) pairs by breaking a covalent bond in the silicon lattice. In a low energy state, the silicon crystal structure consists of atoms tetrahedrally bonded by sharing valence electrons (covalent bonding). A charged particle can break bonds creating "free" electrons and corresponding "free" holes. The electrons and holes are "carriers," or mobile charged particles. The total charge generated is proportional to the energy lost by the charged particle,  $Q \propto \Delta E$ . A charged particle must have enough energy to jump from the valence band to the conduction band. The band gap is dependent on the material, doping, and device configuration. For silicon, the band gap is  $E_g = 1.12$  electron volts (eV). Photon energy  $E(eV)$  can be converted to a wavelength using the following relationship:  $h\nu \geq E_g$ , where  $h = 6.63 \times 10^{-34}$  J-s is Planck's constant,  $\nu = c/\lambda$  is the frequency of the photon, and  $E_g$  is the energy gap of the material. If the photon has less energy than the band gap, it does not promote electrons into the conduction band.

Energetic charged particles, such as electrons, lose kinetic energy (Rutherford scattering or Coulomb scattering) predominately through inelastic collisions with orbital silicon electrons [27]. The electrons either experience a transition to an excited state or to an unbound state into the conduction band (*i.e.*, ionization). Conduction band electrons are collected in the nearest potential well, generating a transient event in an image [13, 36]. Charged particles leave a electron-hole track producing approximately one electron-hole pair for every 3.65 eV of energy absorbed in silicon [27]. The ionizing trail of charge left behind is not a permanent feature and can be erased simply by reading the CCD. This charge deposition by an energetic particle is what this thesis aims to extract from the flight data.

### 2.2 Science Imagers as Radiation Sensors

In space sciences, a measurement of the radiation hits on the detector is common (*e.g.*, [37, 58]). The typical process is to identify radiation and then remove its contribution from the

image signal that one is trying to measure. Techniques for identifying and removing radiation include outlier detection, where pixels that are a certain standard deviation above the surrounding pixels are identified and removed, and boxcar averaging in which pixels with more than a few standard deviations above the mean of the box (*e.g.*, a 5 by 5 pixel box) are replaced with the average of the box [52].

Some studies compare the hit rates in flight data to testing from pre-flight. For the Galileo Solid-State Imaging (SSI) instrument, *Klaasen et al.*, 1997 select 8 images and calculate the measured radiation counts [electrons/sec] and the CCD charge [electrons] compared to the predicted rates. At the time of the study, the Galileo Energetic Particle Detector (EPD) team was able to confirm that the SSI charge rate agreed qualitatively with the EPD (EPD final data products were unavailable at the time *Klaasen's* 1997 paper).

In *Carlson and Hand*, 2015, radiation hits were extracted from the Galileo Near-Infrared Mapping Spectrometer (NIMS) data and the hits were compared to particle transport simulations (Geant4). The full instrument was not modeled; slabs of representative tantalum were used for shielding in the model. The authors varied the shielding and the compared the simulation results to the transient event rates. The authors claim that the results are consistent with those expected at Europa orbit (9.4  $R_J$ ). However, they do not conclude anything about the energy or magnitude of that flux.

In *Grant et al.*, 2010 and 2012, the Chandra X-ray Observatory advanced CCD imaging spectrometer (ACIS) team developed a technique to use the CCDs as radiation monitors. The Electron, Proton, Helium Instrument (EPHIN) is a particle detector on Chandra to monitor the local high-energy particle environment. Elevated temperatures on board have limited EPHIN's effectiveness as a radiation monitor; the signal is dominated by thermal noise. Given the degradation, the ACIS CCDs are used to measure the environment. The charge transfer inefficiency (CTI) for two of the CCDs (one backside-illuminated and one frontside-illuminated) is measured over time [23, 24]. *Grant et al.* use ACIS CTI measurements from early in the mission and compare them to the EPHIN data. The algorithm detects CTI threshold crossings. The algorithm showed good agreement with the EPHIN E1300 channel (electrons with 2.64-6.18 MeV). This technique is the current state of the art for measuring radiation using active imaging CCDs. At the time of writing, the CCDs are not used to try to extract a spectra or flux at a given energy, purely for threshold crossings.

*Li et al. and Burke et al.*, 1997 proposed the use of back-illuminated and front-illuminated CCDs, respectively, for charged-particle spectroscopy. They irradiated a large-area front-illuminated imager with  $\alpha$  particles with energies up to 5.5 MeV and protons up to 13 MeV. This study was not for the purposes of radiation detection in space, rather for diagnostics of inertial confinement fusion implosions. They compared the tests to calculations and found agreement, concluding that CCDs could be used for proton and alpha particle spectroscopy.

In summary, radiation detection is typically limited to spectrometers and radiation hits are dealt with in CCDs as an annoyance that needs to be removed. In some cases, hit rates are computed, such as for the SSI and NIMS [37, 7], but they are not used to infer anything about the space environment. For the Chandra CCDs, radiation information is extracted, but energies and fluxes are not part of the technique in the algorithm. This thesis aims to extract the noise in solid-state devices and use the noise as a measurement of the high-energy radiation environment, including detail of the environment characteristics (energy spectra, particle species, rise/decay-time, flux).

## Chapter 3

# Approach and Methodology

We are developing a technique to extract environment information from a science imager. The goal is to determine the energy (or energies) that the imager is sensitive to and the environment flux at that energy. We simulate electron transport to model the passage of electrons through the instrument to the detector. The number of pixels with hits and the energy deposited in those hits can then be compared with actual observations and used to iterate upon and best-fit or constrain the incident particle flux and energy distribution in the environment. We try to extract a range of energies or an integral energy channel that the imager is sensitive to. For the flux at a given energy, we calculate geometric factors from the simulations that can then be applied to the pixels with hits on the imager.

We will develop and demonstrate the technique using the Galileo Solid-State Imaging (SSI) instrument. Galileo has an energetic particle detector (EPD) which will be used for comparison, along with Pioneer's Geiger Tube Telescope (GTT) for higher energies (up to 31 MeV electrons). Figure 3.1 shows an overview of the approach using the Galileo SSI.

To be able to apply the technique more generally to imagers, we will examine another source of flight data on the Galileo spacecraft, the Near-Infrared Mapping Spectrometer (NIMS). In general, for the analysis, the following information is required:

- For the imager observations, we require: (1) raw images that have not undergone lossy compression, (2) gain factors relating the digital number to electrons, (3) information on dark current and other calibration factors, and (4) detector readout information (line by line, frame modes).
- For the simulations, we require: (1) a model of the key components and detector (geometry and materials), and (2) access to particle transport code (*e.g.*, Geant4).

While it may not be possible to replicate the space environment in the laboratory, we will perform mono-energetic beam tests on a silicon detector to demonstrate that the simulations are validated by and calibrated to the experiment results for mono-energetic beams.

### 3.1 Galileo Solid-State Imaging (SSI) Experiment

The Galileo Solid-State Imaging (SSI) experiment is a high-resolution (1500 mm focal length) system with a spectral range of approximately 375 nm to 1100 nm. The detector is an 800 by 800 pixel virtual-phase, silicon charge-coupled device (CCD). The dimensions of the detector are 12.19 mm x 12.19 mm with a 65.6 pixel per millimeter pixel density. The full-well capacity is 108,000 e<sup>-</sup> (in normal modes) and the noise floor is  $\pm 30$  e<sup>-</sup>. The gain states are given in Table 3.1. Figure 3.2 is a diagram of the Galileo spacecraft and the imaging instruments (labeled in red), including the SSI. For more details on the camera system, detector response, and early in-flight performance, see [4], [37], and references therein.

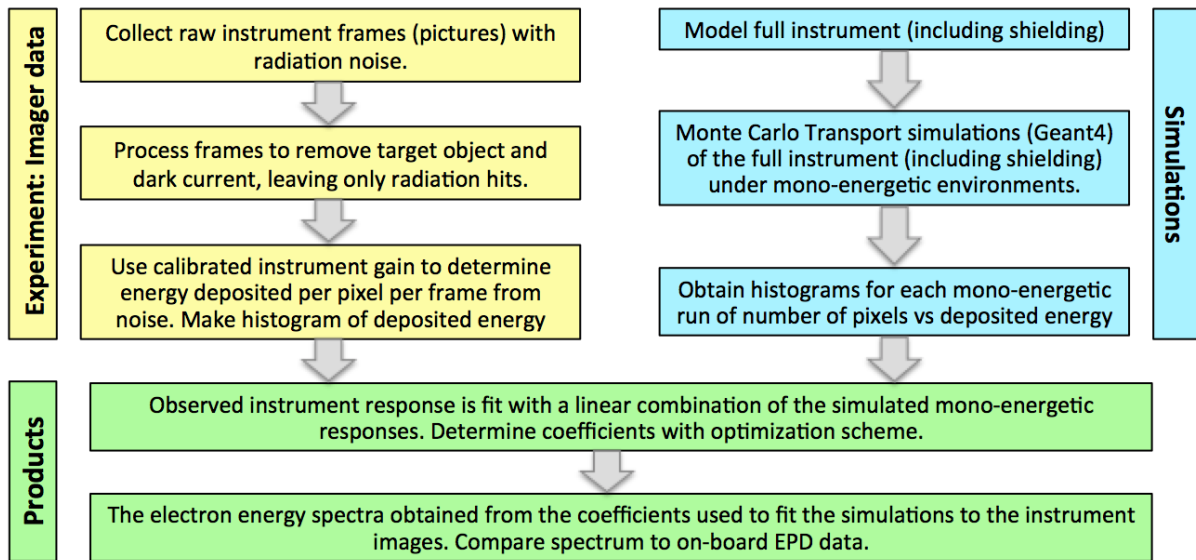


FIGURE 3.1: Approach to extracting high-energy information from the SSI flight data.

### 3.1.1 Experiment: Flight Data

Referring to Figure 3.1 and starting with the SSI data, we collect the raw images and their associated calibration files (dark current, radiometric calibration, blemish, and shutter offset files) from the Planetary Data System<sup>1</sup> (PDS). Due to an anomaly with the Galileo high-gain antenna [Johnson, 1994], a majority of the images were compressed with loss of information. We select the images that have not undergone lossy compression or spike reduction on-board, leaving only 767 out of a total of 4002 (19%) of images for evaluation in this study.

We process the flight data, subtracting the dark current from the imager data and applying the calibrated instrument gain from the image header file. The digital number (DN) ranges from 0 to 255 and the instrument gain converts the DN to electrons. There are four gain states and their factors can be found in Table 3.1. For silicon, the ionization energy needed to create an electron-hole pair is 3.6 eV [49] (*i.e.*, the delta-Energy for an electron to move from the valence band to the conduction band). The processed image is a matrix of energy deposited in each pixel, which can then be binned to form a histogram of energy deposited by the number of pixels.

TABLE 3.1: Gain state for converting digital number to electrons. The gain state ratio factors are found in the calibration files. Uncertainties from the original calibration can be found in the JPL calibration report [35]. Temperatures are in Kelvin (K).

Commanded Gain	Gain State Ratio Factors	Conversion	Notes
0 = Gain 1	1.00	1822 e-/DN	Summation mode only, ~400 K full scale
1 = Gain 2	4.824	377.4 e-/DN	Low gain, ~100 K full scale
2 = Gain 3	9.771	186.5 e-/DN	~40 K full scale
3 = Gain 4	47.135	38.66 e-/DN	High gain, ~10 K full 255 DN scale

Figure 3.4 shows SSI data from an observation of one of Jupiter’s moons, Europa. Figure 3.5a shows the DN as the distance from the center of the moon increases (in pixels). We identify the moon so it can be extracted since radiation hits are not distinguishable from

<sup>1</sup><https://pds-imaging.jpl.nasa.gov/>

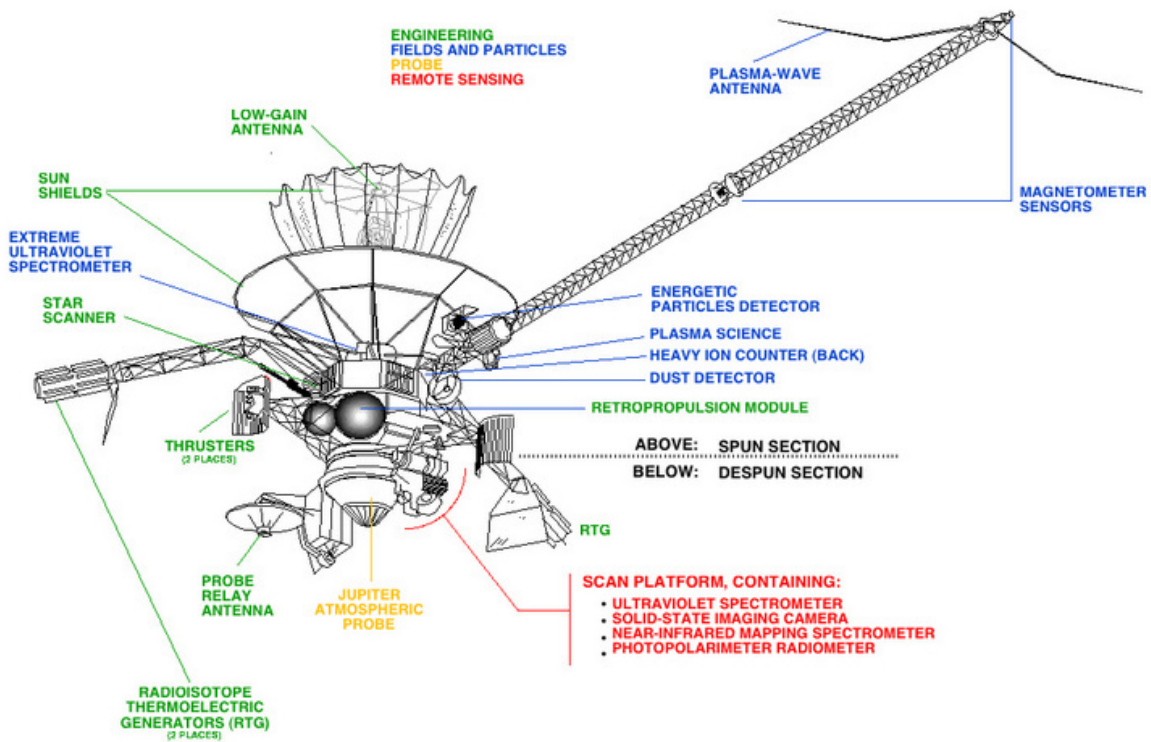


FIGURE 3.2: Diagram of the Galileo spacecraft with the main components and instruments labeled. The SSI is part of the scan platform, to the bottom right of the drawing, labeled in red. The EPD is to the top right of the drawing, labeled in blue. Image source: NASA, 1989, <https://solarsystem.nasa.gov/galleries/galileo-diagram-labeled>.

the source signal. While some of the high (greater than  $DN=120$ ) pixels in the moon part of the observation are likely radiation, they are excluded at the present. For the data plotted in Figure 3.5a, from visual inspection, we remove the data that are less than 95 pixels from the center of the moon. A histogram of the number of pixels with a given DN is plotted in Figure 3.6. The energy deposited in keV is also provided.

FIGURE 3.3: Digital number (DN) to energy deposited conversion for the SSI gain states.

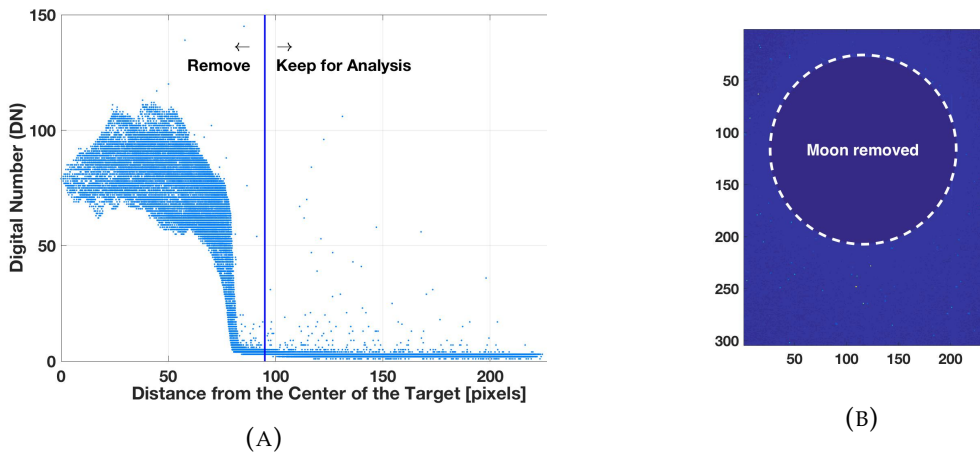
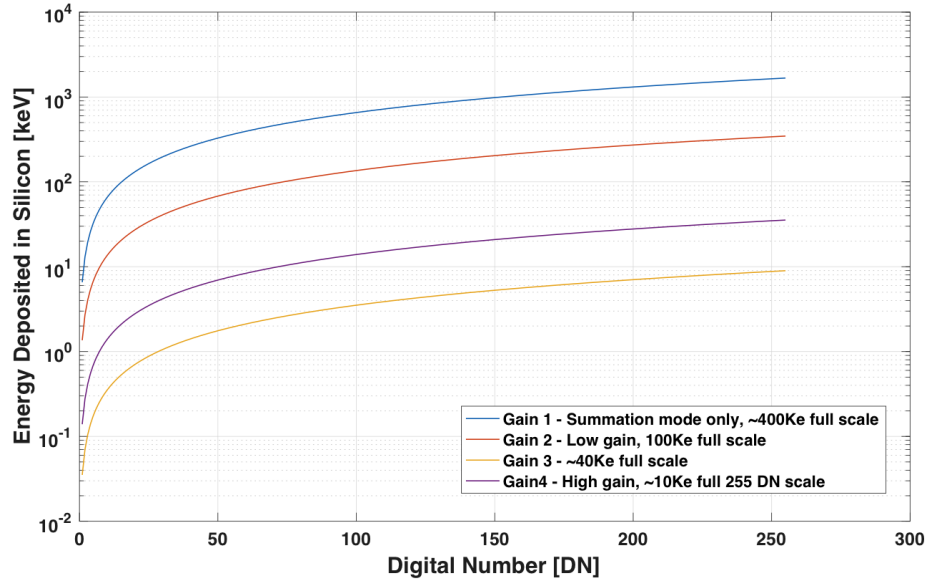


FIGURE 3.5: Removing the target (moon, Europa) from the image. (a) Digital number (DN) as a function of distance from the center of the moon. The vertical line is drawn at 95 pixels from the center of the moon, dividing the moon from the dark sky. (b) Image with the moon subtracted, leaving on the dark sky with radiation hits.

### 3.1.2 Simulations

We simulate electron transport in the SSI to determine the energies of the source particles that can reach the detector (in the form of pixels with hits) and the amount of energy that is deposited in the pixels. I use a Monte Carlo particle transport code called Geant4<sup>2</sup> [1]. Geant4 uses Monte Carlo methods: it does not solve explicit transport equations but obtains results by simulating individual particles and recording their average behavior (results are statistical). Particles are tracked from the source environment to the target (the detector, in this case). Geant4 is capable of modeling all particles relevant to the space environment (electrons, photons, protons, neutrons and heavy ions).

<sup>2</sup><http://geant4.web.cern.ch/geant4/>

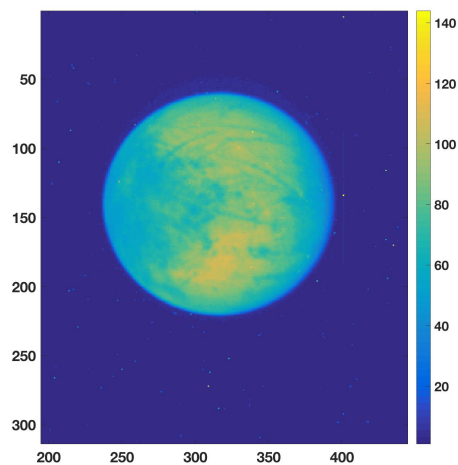


FIGURE 3.4: SSI image of Europa from 2002-01-18 15:16:32.0 in orbit 33. The image was taken as a subset of the  $800 \times 800$  array. The exposure duration is 195.83 ms and the readout is 8.667 s. The gain mode is 100K, or 377.4 e-/DN. The image was taken at  $17.7 R_J$  (L-shell of 17.0). The intensity scale is in digital number (DN).

We model the Galileo SSI instrument in three dimensions, a cut-away visualization of which is shown in Figure 3.7 with labels of the key components [45]. Both the materials and physical placements are accounted for in the geometry. I perform mono-energetic electron runs in Geant4 for energies of 1, 3, 5, 10, 30, 50, 100, and 200 MeV with one billion electrons. The source environment is an isotropic sphere with a radius of 150 cm radiating inward towards the detector, which is located at the center of the sphere. For a simulation of  $1 \times 10^9$  electrons at each energy, I calculate the number of pixels with energy deposited in them. Table 3.2 gives the results for those simulations. For each energy, the number of unique primary and secondary particles and the number of pixels in the 800 by 800 pixel array are recorded. Secondary particles are any order (2nd order, 3rd order, etc.) particles that are not primary particles. Other particles from nuclear reactions such as positrons and gammas can also deposit energy, however their contribution is negligible compared to the electrons; for example, for a one billion 50 MeV electron simulation, 26,252 electrons, 4,236 positrons, and 37 gammas deposit energy. These particles are all accounted for in the Geant4 simulation physics.

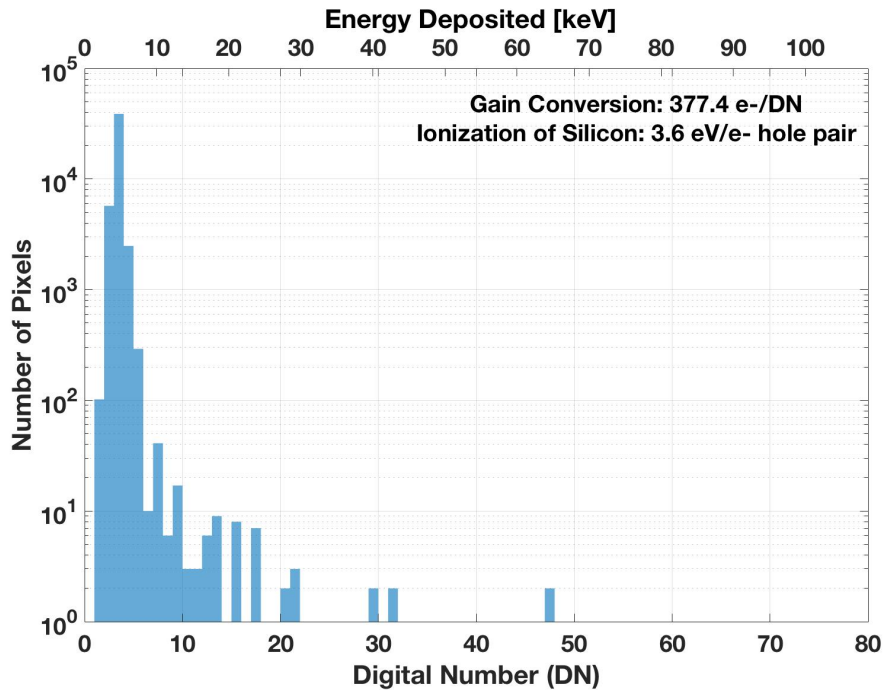


FIGURE 3.6: Histogram of the energy deposited in the moon-removed image. The lower x-axis is the digital number and the upper x-axis labels the corresponding energy deposited in keV.

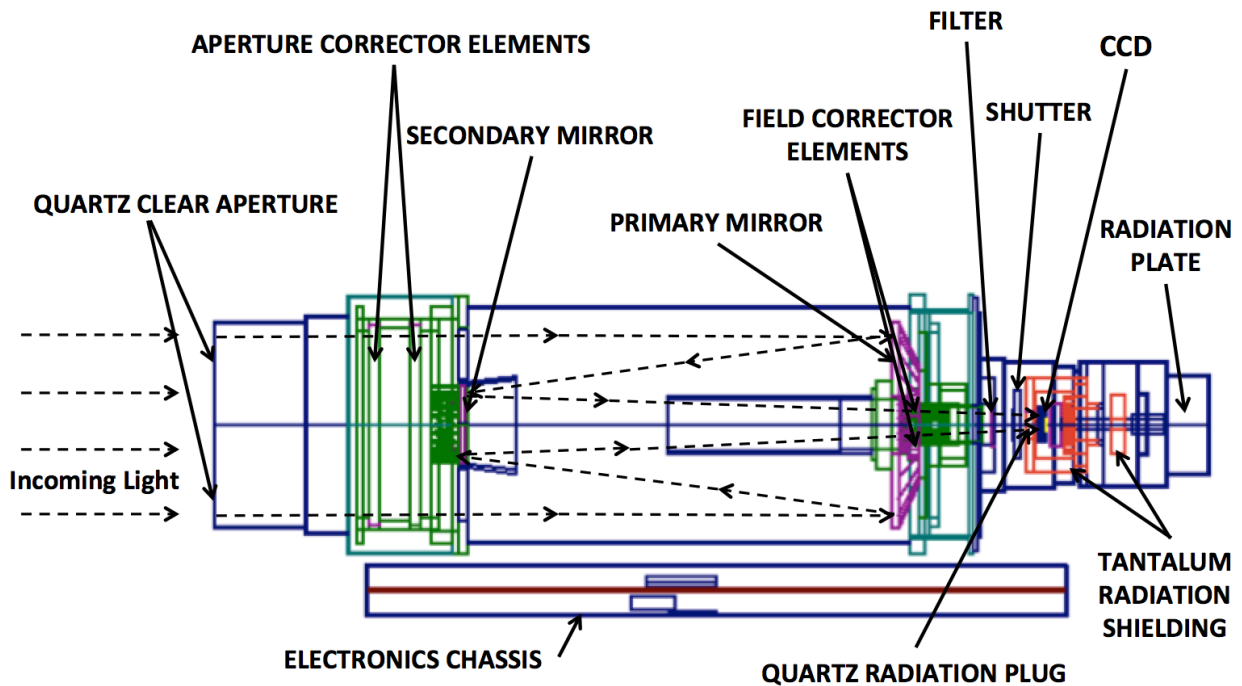


FIGURE 3.7: Cut-away visualization of the geometry built in Geant4 of the SSI. The key components are labeled. The colors correspond to the material of the element (yellow - silicon, dark blue - aluminum, cyan - titanium, green - invar, pink - silica, red orange - tantalum, brown - printed wiring board).

For each of the mono-energetic simulations, we build a histogram of the energy deposited in the detector. Figure 3.8 plots the histograms of energy deposited. We try to

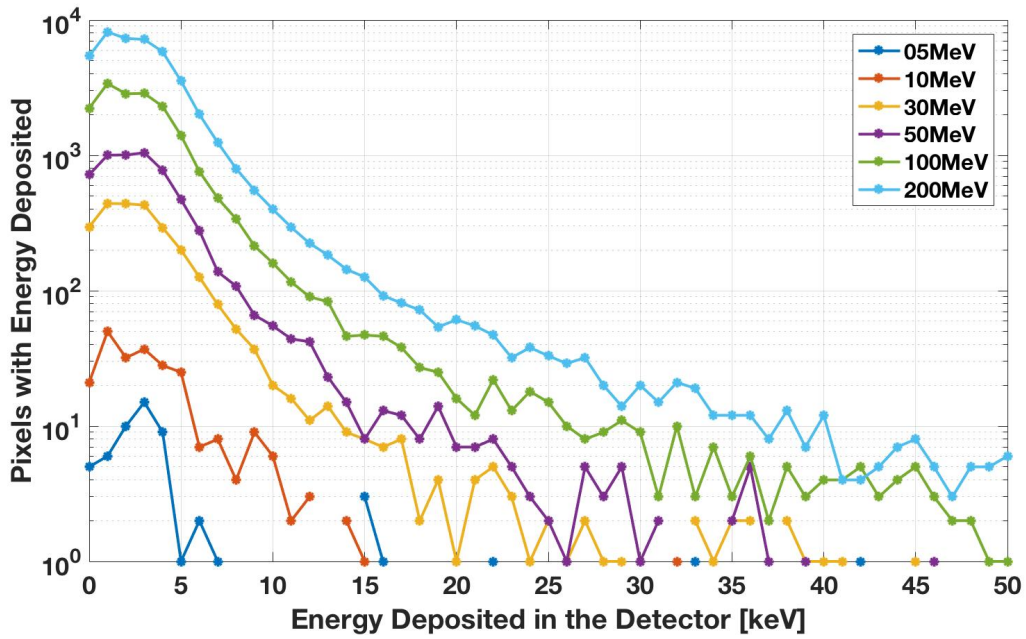


FIGURE 3.8: Histograms of the energy deposited from the Geant4 simulations of 5, 10, 30, 50, 100, and 200 MeV electrons. We set the histogram bin widths to 1 keV.

identify distinctive shapes of the mono-energetic histograms by fitting splines and Gaussians to the histograms. Then, the fitted curves would be used as a basis function and fit to the SSI energy histograms. In other words, for each energy, the multiplicative factor for the curve to match the SSI would translate to the flux for the given energy. The next steps include performing more simulations (repeat each mono-energetic run 5 to 10 times) to be able to place a confidence interval on the energy range for detection and the number of particles of a given energy that reach the detector.

### Preliminary Results - Energy

Referring to Table 3.2, the mono-energetic simulations of 1, 3, and 5 MeV deposit little or no energy on the detector; fewer than 0.009% of pixels are hit. The detection energy for the detector is in the >10 to >50 MeV range. The minimum equivalent shielding of Aluminum for the detector is about 30 mm (or  $\sim 1000$  mils), which was calculated by hand in two dimensions<sup>3</sup>. This corresponds to a dose depth penetration of electrons  $\sim 10$  MeV [12], which is consistent with the simulation findings. Future work for this case study includes refining the cut-off energy and placing a confidence interval on the number.

Looking at Figure 3.8, the shapes of the energy deposition curves for 30 to 200 MeV are similar. In order to better understand why these curves look similar, I plot the energy deposited on the detector as a function of the kinetic energy of the particles at the detector (see Figure 3.9) and find the results are consistent with the stopping power of electrons in silicon. From about 1 to 80 keV, there is roughly a one-to-one ratio between the energy at the detector and the energy deposited. This is because the majority of the lower energy particles are depositing all of their energy on the detector. For  $\geq 100$  keV, the incident energy does not affect the energy deposited on the detector. From about  $10^{-1}$  to  $10^2$  MeV, the stopping power is roughly flat, indicating roughly the same stopping power ( $\text{MeV cm}^2/\text{g}$ ).

<sup>3</sup>This number will be defined more precisely and accurately when we use FASTRAD to find the minimum path to the detector in three dimensions.

TABLE 3.2: Results of Geant4 simulations for particles that reach the SSI detector and deposit energy. The Geant4 simulations are of  $1e9$  electrons with energies 1, 3, 5, 10, 30, 50, 100, and 200 MeV. Columns B and C are the numbers of unique primary and secondary particles that deposit energy on the detector, respectively, and their sum is in Column D. Column E is the total number of pixels with energy deposition ("hits") and Column G is the ratio of particle hits to pixel hits (Column D divided by Column E). Column F is the percentage of the 800 by 800 pixel array that has hits.

A	B	C	D	E	F	G
Energy [MeV]	# Unique Hits from Primaries	# Unique Hits from Secondaries	Total Unique Particle Hits (B + C)	# of Pixels with Hits	Percent of 800 x 800 detector	Particle to Pixel Hits (G / E)
1	0	0	0	0	0.00	0
3	0	6	6	11	0.002	0.55
5	1	19	20	57	0.01	0.35
10	37	91	128	241	0.04	0.53
30	329	1063	1392	2529	0.40	0.55
50	626	2544	3170	5910	0.92	0.54
100	1197	8063	9260	17742	2.77	0.52
200	1975	20573	22548	44281	6.92	0.51

The continuous-slowing-down approximation (CSDA) range for 90 keV electrons is  $\sim 0.4734$  g/cm<sup>2</sup> [55]. Dividing by the density of silicon (2.33 g/cm<sup>3</sup>), that gives an approximate thickness of silicon of 20  $\mu$ m, which is very close to the 15  $\mu$ m thickness of the detector sensitive layer in the model, showing that the model physics are self-consistent.

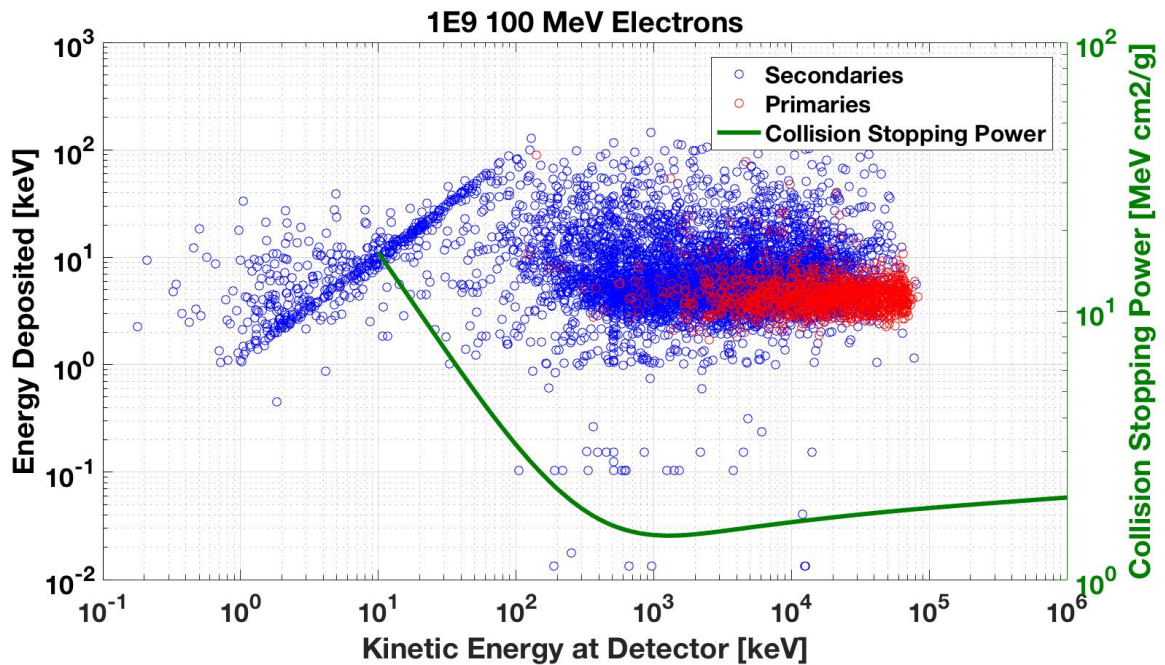


FIGURE 3.9: Energy deposited in the detector (left y-axis) as a function of the energy of the particle at the detector for 100 MeV electrons. The primary particles are red circles and the secondaries are blue circles. The collision stopping power is plotted in green on the right y-axis.

### Preliminary Results - Flux Measurement

The only information from the SSI flight data is the number of pixels with hits with certain digital numbers. We use the mono-energetic Geant4 simulations (since the flux was our input to Geant4) to determine the geometric factors. To convert the number of pixels with energy deposited to the flux in the environment, there are several steps, in terms of "geometric factors," which are a combination of efficiencies and the physical view factor of the detector. The number of particles that reach the detector and deposit energy depends on: the energy of the source particles, the number of source particles, the surface area of the source sphere (in  $4\pi$  space), the shielding materials (response to energetic particles, *i.e.*, generation of secondaries) and geometry (thickness), the surface area of the detector, and other detector properties.

Referring to the mono-energetic simulation results in Table 3.2, from the total number of pixels with energy deposited (column E) number, we seek the number of particles of a given energy in the environment. Combining the number of unique primaries and secondaries that reach the detector and deposit energy (column D), we can find the approximate number of particles given a certain number of pixels with hits. The pixel count rate is  $R_0$  and the particle count rate is  $R_1$ , scaled by the ratio of particles to pixels  $G_1$ , found in column G, using the following equation:

$$R_1 = R_0 G_1 \quad (3.1)$$

From the table, ignoring 1, 3, and 5 MeV, there is a common factor of  $G_1 = 0.53 \pm 0.014$  (95% confidence) relating the number of pixels to the number of particles. This factor will be different for a given instrument, and must be calculated through analysis of charged particle transport simulations, as shown here.

For the Geant4 simulations, we know the input fluence (time for particle interactions is assumed to be negligible):  $N = 1 \times 10^9$  source electrons, coming from a  $4\pi$  sphere of radius  $r = 150 \text{ cm}^2$ , so we can write the particle fluence  $f_0$  from the simulation as:

$$f_0 = \frac{N}{4\pi \times (4\pi r^2)} = \frac{1 \times 10^9}{4\pi \times (4\pi (150\text{cm})^2)} \quad [\#/ \text{cm}^2 / \text{s} / \text{sr}] \quad (3.2)$$

To represent the real environment,  $f_0$  needs to be multiplied by four: a factor of two because the simulation is a sphere with particles going in (real environment is in and out), and another factor of two because the simulation is a cosine (real environment is isotropic). Since we know the fluence  $f_0$  of the mono-energetic simulations and the converted count rate  $R_1$  for each energy, we can calculate the second scale factor  $G_2$ , which will also be a function of energy  $E$ .  $G_2$  has units of steradian:

$$\begin{aligned} R_1 &= f_0 G_2(E) \\ G_2(E) &= \frac{R_1}{f_0} \end{aligned} \quad (3.3)$$

For each pixel count rate in the mono-energetic Geant4 simulations (see Table 3.2, we calculate the scale factors,  $G_2(E)$ , which are listed in Table 3.3.

#### 3.1.3 Example: SSI Observation 5101r, Orbit 22

As an example, we select an image taken in orbit 22 (1999-08-12T19:13:10.828z) at 9.4  $R_J$  of Amalthea. After Amalthea is identified, removed, and the dark current is subtracted, we find 295 out of 4161 pixels with hits (7.09%). The integration time is 62.5 ms and the readout time is 8.667 s (the shutter contributes very little to blocking the high-energy electrons, so

TABLE 3.3: Geometric scale factor  $G_2$  that relates the particle count rate at the detector to the environmental flux for a given energy.

Energy [MeV]	# Geometric scale factor, $G_2$ [sr]
5	0.0036
10	0.019
30	0.827
50	1.93
100	5.80
200	14.5

we include the readout time<sup>4</sup>). The pixel hit rate per unit area  $R_0$  over the image is:

$$\begin{aligned}
 R_0 &= \frac{295\text{px}}{4161\text{px}} \times \frac{1\text{px}}{15\mu\text{m}^2} = 31510 \quad [\text{px}/\text{cm}^2] \\
 &= \frac{31510[\text{px}/\text{cm}^2]}{62.5 \times 10^{-3}\text{s} + 8.667\text{s}} \quad [\text{px}/\text{cm}^2/\text{s}] \\
 &= 3610 \quad [\#/ \text{cm}^2/\text{s}]
 \end{aligned}$$

Converting to the particle rate per unit area, using  $G_1 = 0.53$  and Equation 3.1,

$$\begin{aligned}
 R_1 &= 3610(0.53) \quad [\#/ \text{cm}^2/\text{s}] \\
 &= 1913 \quad [\#/ \text{cm}^2/\text{s}]
 \end{aligned}$$

This particle count rate per unit area,  $R_1$ , is from particles in the environment from all energies (above a certain threshold, around 10 MeV and greater). Using  $G_2$  in Table 3.3 and Equation 3.3, we calculate the flux assuming all particles are from 10 MeV source particles:  $f = 2.43 \times 10^4 [\frac{1}{\text{cm}^2 \text{ s sr}}]$ . This places an upper limit on the flux since some of the particles will be from higher and lower energies and will not contribute to the 10 MeV flux. There is not a corresponding EPD measurement at the time of the observation, so we identify the average integral flux for the same distance ( $R_J = 9.4$ ) and the same spacecraft latitude ( $0.633^\circ$ ). The EPD DC3 flux (>11 MeV flux) is  $2.6 \times 10^5 [\frac{1}{\text{cm}^2 \text{ s sr}}]$ . This is consistent with the calculated approximate differential flux within an order of magnitude with the flux derived from the SSI observation.

The next steps include processing the remainder of the SSI images and extracting the radiation noise. For each image (at a given distance from Jupiter), we will calculate the differential environmental flux using the technique described in this paper. We will compare the flux values to the Galileo EPD and models of the Jovian environment. We will also perform more mono-energetic electron simulations to place error bars on the geometric scale factors for the flux and to better determine the low energy cut-off of the detector.

## 3.2 Galileo Near Infrared Imaging Spectrometer (NIMS)

To demonstrate the technique with another instrument, we will analyze the Galileo Near Infrared Mapping Spectrometer (NIMS). NIMS is a combination of an imager and spectrometer and is sensitive to 0.7 to 5.2  $\mu\text{m}$ , overlapping with the SSI [8]. The detector consists of 17 individual imaging elements (15 indium antimonide and 2 silicon pixels). Each of the photodiode detectors has an active area of 0.2 mm by 0.2 mm. "Spike" files have already

<sup>4</sup>The shutter includes two aluminum cylinders of Aluminum with thicknesses of 5 mm and 2 mm.

been generated for the NIMS on-orbit data (see [7]), which could reduce the processing required, although a more detailed look at the algorithm is required. The spike files have hit information for each pixel and the relative energy deposition (DN) [7]. The instrument will need to be modeled in Geant4 and simulations performed to determine the sensitive energy range and to calculate the necessary scaling factors for constraining the flux.

The hit rate varies for each of the detector<sup>5</sup>, and seems to increase as a function of pixel number. This could be due to the asymmetrical shielding the instrument would receive from the configuration of the pixels (see Figure 3.10). The differential shielding is encouraging as it may be possible to extract multiple energy channels.

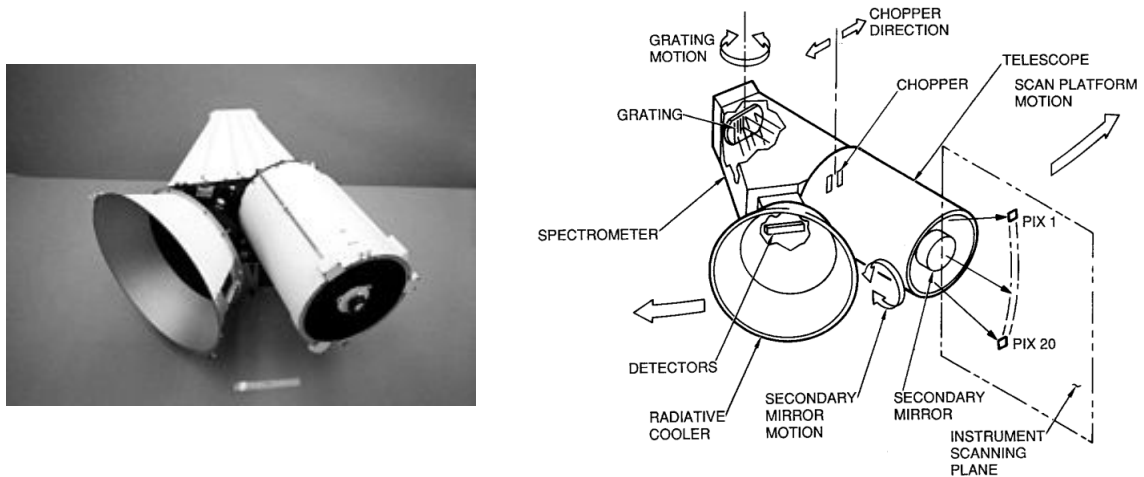


FIGURE 3.10: Photograph (left) and labeled diagram (right) of the NIMS instrument from *Carlson et al., 2012*. The telescope is on the right, the radiative cooler is facing left and the spectrometer is behind.

### 3.3 Validation

#### 3.3.1 Galileo Energetic Particle Detector

To validate the technique developed, we compare the results to the Galileo Energetic Particle Detector (EPD). The EPD provide  $4\pi$  angular coverage spectral measurement for  $Z \geq 1$  ions, for electrons, and for the elemental species helium through iron. The EPD consists of two telescopes called the Low Energy Magnetospheric Measurement System (LEMMS) and the Composition Measurement System (CMS). The LEMMS is the most applicable for our studies. The LEMMS detector head is a double-ended telescope containing eight heavily shielded detectors providing measurements of electrons from 15 keV to  $>11$  MeV, and ions from 22 keV to  $\sim 55$  MeV, in 32 rate channels. Of the LEMMS channels, the most important one for our study of the SSI is the DC3 electron channel, which is an integral flux measurement  $>11$  MeV. More information on the EPD can be found in [56].

<sup>5</sup>Personal communications with Michael Mercury at JPL in April 2017.

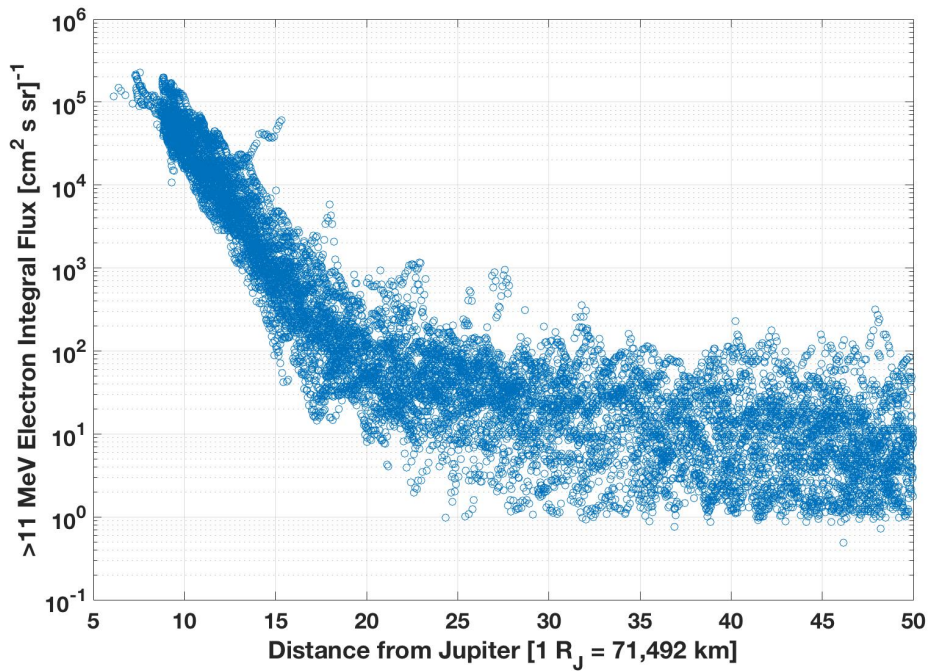


FIGURE 3.11: Galileo EPD >11 MeV integral flux channel (DC3) as a function of distance from Jupiter in R<sub>J</sub>.

Ideally, the technique developed in this thesis will be capable of making comparable measurements to the EPD. There is a spread in the EPD data, which comes from variations in the environment and statistical uncertainties in the measurement. Jun et al. find a log-normal fit to the EPD data DC3 integral flux, shown in Figure 3.11 as a solid black line, as a function of the distance from Jupiter (in R<sub>J</sub>). The dashed lines represent the 1-, 2-, and 3-sigma on the log-normal fit [32]. We will add SSI images to the analysis and error bars with the goal of having agreement within the spread of the EPD measurements.

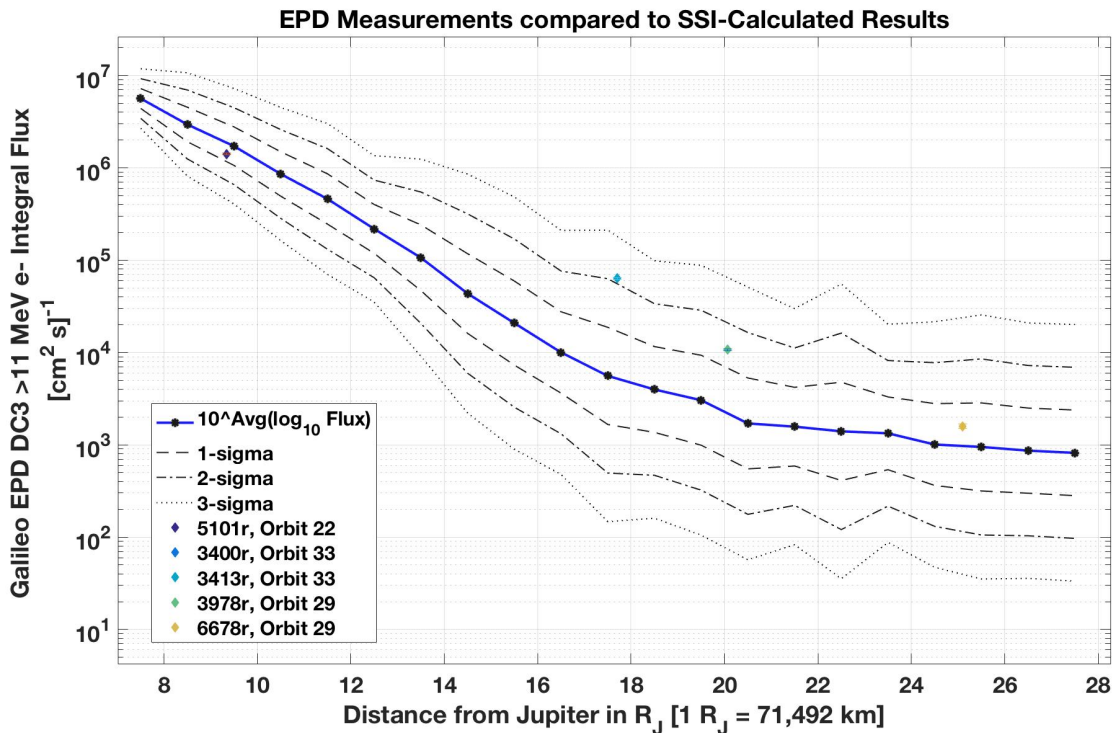


FIGURE 3.12: Galileo EPD >11 MeV integral flux channel as a function of distance from Jupiter in  $R_J$ . The results from five SSI images analyzed to date are plotted on top of the EPD measurements. The error bars for each SSI image are within the size of the data point.

### 3.3.2 In-Lab Testing

While an accurate simulation of the space radiation environment is not possible in the laboratory (high-energy beams used in lab testing are mono-energetic sources, not energy distributions), we will examine the response of a semiconductor device under different amounts of shielding to at least three mono-energetic electron beams. While not required for validation of the technique, these tests will strengthen the confidence in the mono-energetic Geant4 simulations and will serve as a learning opportunity for A. Carlton.

The NASA Jet Propulsion Laboratory (JPL, Pasadena, CA) Natural Space Environments group (5132) is planning to test a silicon semiconductor device (final device TBD) for electrons with energies up to 2 MeV in the JPL Dynamitron. Due to the financial and logistical constraints, A. Carlton plans to support and contribute to that testing run<sup>6</sup>. We will test the detector with no shielding to start with, and then we will add TBD shielding to assist with the validation of the mono-energetic simulations. The basic elements of the test set up are the silicon detector, a pre-amplifier (adjusting the feedback resistor and capacitor to match the detector) and a digitizer for the output signals of the preamplifier. Test planning, modeling of the test configuration, electron beam tests, and analysis of results will take place during the summer of 2017.

<sup>6</sup>A. Carlton will not need to financially contribute to the cost of the hardware or the beam time, only her physical travel to NASA JPL, which will be supported by her NASA Space Technology Research Fellowship (NSTRF). A. Carlton will contribute to the test plan, design, modeling in Geant4, and will be physically assisting the day of the testing.

### 3.4 Descope Options

If it is not possible to extract an integral energy channel from either the SSI or NIMS instruments (*e.g.*, the information extracted does not agree with the EPD), we will augment the null result with additional analyses of non-traditional sources of radiation information. We will analyze housekeeping telemetry from Galileo. We will extract atypical events (change points, transients) and compare the events to the EPD and known spacecraft upsets [16]. Another source of environment data could come from Galileo's Ultra-Stable Oscillators (USOs). USO frequency shifts correspond to radiation dose.

## Chapter 4

# Expected Contributions

- Invent a technique and design a generalized procedure to extract high-energy (>1 MeV) electron environment information from solid-state detectors.
  - Demonstrate how to find at least one integral energy channel from the Galileo Solid-State Imaging instrument.
  - Demonstrate how to find at least one integral energy channel from the Galileo Near-Infrared Mapping Spectrometer (NIMS).
  - Demonstrate agreement with the Galileo Energetic Particle Detector (EPD).
  - Analyze results compared to current Jovian radiation models (GIRE-2).
- Test solid-state detector in electron beams to validate Geant4 modeling physics.
- Compose recommendations and requirements for testing, calibration, and operational procedures for an instrument on the Europa Clipper mission in order to use the technique developed in this thesis.



## Chapter 5

# Status and Proposed Schedule

### 5.1 Classes and Degree Milestones

Tables 5.1 and 5.2 show my coursework and degree milestones to date, respectively, and the plan for completing the remaining coursework and milestones.

TABLE 5.1: This table shows my coursework to date as well as the expected course this fall. I am on track to meet all academic doctoral requirements.

Timeline	Work	Req.	Progress
Fall 2013	16.413 Intro. to Autonomy & Decision Making	major	completed
Fall 2014	16.851 Satellite Engineering	major	completed
Fall 2014	16.910 Intro. to Numerical Simulation	minor	completed
Spring 2015	16.363 Communications Systems	major	completed
Spring 2015	16.89 Space Systems Engineering	major	completed
Spring 2015	22.16 Nuclear Technology and Society	major	completed
Fall 2016	16.899 Systems Engineering of FLARE Project	major	completed
Fall 2016	16.343 Sensors and Instrumentation	minor	ongoing
Fall 2017	8.701 Nuclear and Particle Physics	minor	planned

TABLE 5.2: This table shows my degree milestones to date and anticipated milestones. Dates in italics are tentative. I am on track to meet all degree requirements.

September 2014	Began studies at MIT
January 2016	Research and Field Qualifying Exams
May 2016	Masters thesis and degree
September 2016	Formation of doctoral committee
December 2016	Committee Meeting #1
March 2017	Committee Meeting #2
May 2017	Thesis Proposal Defense
<i>Fall 2017</i>	<i>Committee Meeting #3</i>
<i>Spring 2018</i>	<i>Committee Meeting #4</i>
<i>Summer 2018</i>	<i>Committee Meeting #5</i>
<i>Fall 2018</i>	<i>Thesis Defense</i>

## 5.2 Research Schedule

### *April-May 2017*

- Complete the model of the SSI in Geant4, perform mono-energetic simulations.
- Determine the energy range of source particle energies that the detector is sensitive to.
- Determine scaling factors for extracting the flux (at a given energy) given the number of pixels with radiation hits.
- Testing: support test plan and part procurement.
- Present at the Applied Space Environments Conference in Huntsville, AL (15-19 May 2017).
- Complete additional mono-energetic simulations of the SSI in Geant4 to define confidence interval on energy and flux measurements.

### *Summer 2017*

- Submit paper on masters research.
- Testing:
  - June: Model instrument and test configuration in Geant4.
  - July: Perform tests in lab.
  - August: Post-process results.

### *Fall 2017*

- Complete extraction of radiation information from SSI flight data. Comparison to Geant4 simulations for determination of flux environment at a given energy. Comparison of results to EPD data and GIRE-2.
- Begin analysis of NIMS data. Determine how to extract the energy and hit rate information from the images.
- Present progress at the American Geophysical Union in New Orleans, LA (December 2017).

### *Spring 2018*

- Modeling of NIMS in Geant4. Perform mono-energetic simulations.
- Write up SSI results for publication.
- Conference presentation (TBD).

### *Summer 2018*

- Comparison of NIMS results to EPD, GIRE-2, and to the results from SSI.
- Write thesis.

*Fall 2018*

- Write thesis.
- Conference presentation or paper (TBD).
- Defend thesis and graduate.



# Bibliography

- [1] S. Agostinelli et al. “Geant4—a simulation toolkit”. In: *Nuclear Instruments and Methods in Physics Research Section A: Accelerators, Spectrometers, Detectors and Associated Equipment* 506.3 (2003), pp. 250–303. ISSN: 0168-9002. DOI: [http://doi.org/10.1016/S0168-9002\(03\)01368-8](http://doi.org/10.1016/S0168-9002(03)01368-8). URL: <http://www.sciencedirect.com/science/article/pii/S0168900203013688>.
- [2] Fran Bagenal, Timothy E. Dowling, and William McKinnon, eds. *Cambridge Planetary Science*. ISBN 0-521-81808-7. Cambridge University Press, 2004.
- [3] Daniel N. Baker. “The Occurrence of Operational Anomalies in Spacecraft and Their Relationship to Space Weather”. In: *IEEE Transactions on Plasma Science* 28.6 (2000). doi:10.1109/27.902228.
- [4] Michael J. S. Belton et al. “The Galileo Solid-State Imaging experiment”. In: *Space Science Reviews* 60.1 (1992), pp. 413–455. ISSN: 1572-9672. DOI: 10.1007/BF00216864. URL: <http://dx.doi.org/10.1007/BF00216864>.
- [5] S. J. Bolton et al. “Ultra-relativistic electrons in Jupiter’s radiation belts”. In: *Nature* 415.6875 (Feb. 2002), pp. 987–991. URL: <http://dx.doi.org/10.1038/415987a>.
- [6] B. E. Burke et al. “Use of charge-coupled device imagers for charged-particle spectroscopy”. In: *Review of Scientific Instruments* 68.1 (1997), pp. 599–602. DOI: 10.1063/1.1147663. URL: <http://dx.doi.org/10.1063/1.1147663>.
- [7] R. W. Carlson and K. P. Hand. “Radiation Noise Effects at Jupiter’s Moon Europa: In-Situ and Laboratory Measurements and Radiation Transport Calculations”. In: *IEEE Transactions on Nuclear Science* 62.5 (Oct. 2015), pp. 2273–2282. ISSN: 0018-9499. DOI: 10.1109/TNS.2015.2460674.
- [8] R. W. Carlson et al. “Near-Infrared Mapping Spectrometer experiment on Galileo”. In: *Space Science Reviews* 60.1 (1992), pp. 457–502. ISSN: 1572-9672. DOI: 10.1007/BF00216865. URL: <http://dx.doi.org/10.1007/BF00216865>.
- [9] Dakai Chen et al. “The Effects of ELDRS at Ultra-Low Dose Rates”. In: *IEEE Radiation Effects Data Workshop*. doi:10.1109/REDW.2010.5619506. Denver, CO, July 2010.
- [10] Christopher F. Chyba and Cynthia B. Phillips. “Possible Ecosystems and the Search for Life on Europa”. In: *Proceedings of the National Academy of Sciences of the United States of America* 98.3 (2001), pp. 801–804. ISSN: 00278424. URL: <http://www.jstor.org/stable/3054775>.
- [11] John F. Cooper et al. “Energetic Ion and Electron Irradiation of the Icy Galilean Satellites”. In: *Icarus* 149.1 (2001), pp. 133–159. ISSN: 0019-1035. DOI: <http://dx.doi.org/10.1006/icar.2000.6498>. URL: <http://www.sciencedirect.com/science/article/pii/S0019103500964984>.
- [12] E.J. Daly et al. “Space Environment Analysis: Experience and Trends”. In: *Environment Modelling for Space-based Applications, Symposium Proceedings (ESA SP-392)*. 10.1007/978-94-015-9395-3. Noordwijk, The Netherlands, Sept. 1996.

- [13] Taher Daud et al. "Charge-Coupled-Device Response To Electron Beam Energies Of Less Than 1 keV up to 20 keV". In: *Optical Engineering* 26.8 (1987). DOI: 10.1117/12.7974138. URL: <http://dx.doi.org/10.1117/12.7974138>.
- [14] Neil Divine and H. B. Garrett. "Charged particle distributions in Jupiter's magnetosphere". In: *Journal of Geophysical Research: Space Physics* 88.A9 (1983), pp. 6889–6903. ISSN: 2156-2202. DOI: 10.1029/JA088iA09p06889. URL: <http://dx.doi.org/10.1029/JA088iA09p06889>.
- [15] Joseph Fennell et al. *Spacecraft Charging: Observations and Relationships to Satellite Anomalies*. Aerospace Report TR-2001(8570)-5. El Segundo, CA: Aerospace Corporation, 2001.
- [16] Paul D. Fieseler, S. M. Ardalan, and A. R. Frederickson. "The radiation effects on Galileo spacecraft systems at Jupiter". In: *IEEE Transactions on Nuclear Science* 49.6 (2002). doi:10.1109/TNS.2002.805386.
- [17] Arthur R. Frederickson. "Upsets Related to Spacecraft Charging". In: *IEEE Transactions on Nuclear Science* 23.2 (Apr. 1996). doi:10.1109/23.490891, pp. 426–441.
- [18] Henry B. Garrett et al. "A revised model of Jupiter's inner electron belts: Updating the Divine radiation model". In: *Geophysical Research Letters* 32.4 (2005). L04104. ISSN: 1944-8007. DOI: 10.1029/2004GL021986. URL: <http://dx.doi.org/10.1029/2004GL021986>.
- [19] Henry B. Garrett et al. *Galileo Interim Radiation Electron Model: Update–2012, JPL Publication 12-9*. Tech. rep. Pasadena, CA: Jet Propulsion Laboratory, National Aeronautics and Space Administration, 2012.
- [20] Henry B. Garrett et al. *Galileo Interim Radiation Model, JPL Publication 03-006*. Tech. rep. Pasadena, CA: Jet Propulsion Laboratory, National Aeronautics and Space Administration, 2002.
- [21] Henry B. Garrett et al. "The Jovian Charging Environment and Its Effects – A Review". In: *IEEE Transactions on Plasma Science* 40.2 (Feb. 2012), pp. 144–154. ISSN: 0093-3813. DOI: 10.1109/TPS.2011.2171369.
- [22] Barry Goldstein et al. "Europa Clipper Update". Presentation at the Europa Clipper OPAG, unpublished. Jan. 2014.
- [23] C. E. Grant et al. "Using ACIS on the Chandra X-ray Observatory as a particle radiation monitor". In: *Space Telescopes and Instrumentation 2010: Ultraviolet to Gamma Ray. Edited by Arnaud 7732* (2010), p. 80. ISSN: 0277786X. DOI: 10.1117/12.857629. arXiv: arXiv:1007.4185v1. URL: <http://adsabs.harvard.edu/cgi-bin/nph-data{}?query=bibcode=2010SPIE.7732E..80G{}&link{}type=ABSTRACT>.
- [24] C. E. Grant et al. "Using ACIS on the Chandra X-ray Observatory as a particle radiation monitor II". In: *Space Telescopes and Instrumentation 2012: Ultraviolet to Gamma Ray* 8443 (Sept. 2012). ISSN: 844311. DOI: 10.1117/12.925467. URL: <http://dx.doi.org/10.1117/12.925467>.
- [25] P. Hand et al. "Astrobiology and the potential for life on Europa". In: *Europa*. Space Science Series. University of Arizona Press, 2009. Chap. 23?, pp. 589–629. ISBN: 9780816528448. URL: <https://books.google.com/books?id=Jpcz2UoXejgC>.
- [26] Daniel Hastings and Henry Garrett. *Spacecraft-Environment Interactions*. Cambridge Atmospheric and Space Science Series. Cambridge, UK: Cambridge University Press, 1996.
- [27] James R. Janesick. *Scientific Charge-Coupled Devices*. Vol. PM83. Bellingham, Washington: SPIE Press, Jan. 2001.

- [28] R.E. Johnson et al. "Composition and detection of Europa's sputter-induced atmosphere". In: *Europa*. Space Science Series. University of Arizona Press, 2009. Chap. 20, pp. 507–527. ISBN: 9780816528448. URL: <https://books.google.com/books?id=Jpcz2UoXejgC>.
- [29] R.E. Johnson et al. "Radiation effects on the surfaces of the Galilean satellites". In: *Jupiter: The Planet, Satellites and Magnetosphere*. Ed. by Fran Bagenal, Timothy E. Dowling, and William McKinnon. Cambridge University Press, 2004. Chap. 20, pp. 485–512.
- [30] T. V. Johnson and L. A. Soderblom. "Volcanic Eruptions on Io: Implications for Surface Evolution and Mass Loss". In: *IAU Colloq. 57: Satellites of Jupiter*. Ed. by D. Morrison. 1981, p. 634.
- [31] NASA JPL/Caltech. "NASA Juno Image Gallery". URL: [https://www.nasa.gov/mission\\_pages/juno/images/index.html](https://www.nasa.gov/mission_pages/juno/images/index.html).
- [32] Insoo Jun et al. "Statistics of the variations of the high-energy electron population between 7 and 28 jovian radii as measured by the Galileo spacecraft". In: *Icarus* 178.2 (2005). Jovian Magnetospheric Environment Science, pp. 386–394. ISSN: 0019-1035. DOI: <https://doi.org/10.1016/j.icarus.2005.01.022>. URL: <http://www.sciencedirect.com/science/article/pii/S0019103505002253>.
- [33] Krishan K. Khurana and Hannes K. Schwarzl. "Global structure of Jupiter's magnetospheric current sheet". In: *Journal of Geophysical Research: Space Physics* 110.A7 (2005). A07227, n/a–n/a. ISSN: 2156-2202. DOI: [10.1029/2004JA010757](https://doi.org/10.1029/2004JA010757). URL: <http://dx.doi.org/10.1029/2004JA010757>.
- [34] Krishan K. Khurana et al. "The Configuration of Jupiter's Magnetosphere". In: *Jupiter: The Planet, Satellites and Magnetosphere*. Ed. by Fran Bagenal, Timothy E. Dowling, and William McKinnon. Cambridge University Press, 2004. Chap. 24, pp. 559–616.
- [35] Ken Klaasen. *Galileo solid-state imaging subsystem calibration report: part 2*. JPL Document 1625-210. Pasadena, CA: California Institute of Technology, Jet Propulsion Laboratory, 1993.
- [36] Kenneth P. Klaasen, Maurice C. Clary, and James R. Janesick. "Charge-Coupled Device Television Camera For Nasa's Galileo Mission To Jupiter". In: *Optical Engineering* 23.3 (1984). DOI: [10.1117/12.7973290](https://doi.org/10.1117/12.7973290). URL: <http://dx.doi.org/10.1117/12.7973290>.
- [37] Kenneth P. Klaasen et al. "Inflight performance characteristics, calibration, and utilization of the Galileo solid-state imaging camera". In: *Optical Engineering* 36.11 (1997), pp. 3001–3027. DOI: [10.1117/1.601525](https://doi.org/10.1117/1.601525). URL: <http://dx.doi.org/10.1117/1.601525>.
- [38] Norbert Krupp et al. "Dynamics of the Jovian Magnetosphere". In: *Jupiter: The Planet, Satellites and Magnetosphere*. Ed. by Fran Bagenal, Timothy E. Dowling, and William McKinnon. Cambridge University Press, 2004. Chap. 25, pp. 617–638.
- [39] C. K. Li et al. "Charged-coupled devices for charged-particle spectroscopy on OMEGA and NOVA". In: *Review of Scientific Instruments* 68.1 (1997), pp. 593–595. DOI: [10.1063/1.1147661](https://doi.org/10.1063/1.1147661). URL: <http://dx.doi.org/10.1063/1.1147661>.
- [40] Giles M. Marion et al. "The Search for Life on Europa: Limiting Environmental Factors, Potential Habitats, and Earth Analogues". In: *Astrobiology* 3.4 (July 2003). doi:10.1089/15311070332273 pp. 785–811.

- [41] Robert T. Pappalardo et al. *Europa*. Space Science Series. University of Arizona Press, 2009. ISBN: 9780816528448. URL: <https://books.google.com/books?id=Jpcz2UoXejgC>.
- [42] C. Paranicas et al. “Europa’s Radiation Environment and Its Effects on the Surface”. In: *Europa*. Space Science Series. University of Arizona Press, 2009. Chap. 21, pp. 529–544. ISBN: 9780816528448. URL: <https://books.google.com/books?id=Jpcz2UoXejgC>.
- [43] Imke de Pater and David E Dunn. “[VLA] observations of Jupiter’s synchrotron radiation at 15 and 22 {GHz}”. In: *Icarus* 163.2 (2003), pp. 449–455. ISSN: 0019-1035. DOI: [http://dx.doi.org/10.1016/S0019-1035\(03\)00068-X](http://dx.doi.org/10.1016/S0019-1035(03)00068-X). URL: <http://www.sciencedirect.com/science/article/pii/S001910350300068X>.
- [44] G. Wesley Patterson, Chris Paranicas, and Louise M. Prockter. “Characterizing electron bombardment of Europa’s surface by location and depth”. In: *Icarus* 220.1 (2012), pp. 286–290. ISSN: 0019-1035. DOI: <http://dx.doi.org/10.1016/j.icarus.2012.04.024>. URL: <http://www.sciencedirect.com/science/article/pii/S0019103512001662>.
- [45] J. Perl. *HepRep: a Generic Interface Definition for HEP Event Display Representables*. Tech. rep. SLAC-PUB-8332. Palo Alto, CA: Stanford University, 2000.
- [46] Cynthia B. Phillips and Robert T. Pappalardo. “Europa Clipper Mission Concept: Exploring Jupiter’s Ocean Moon”. In: *Eos, Transactions American Geophysical Union* 95.20 (2014), pp. 165–167. ISSN: 2324-9250. DOI: [10.1002/2014EO200002](http://dx.doi.org/10.1002/2014EO200002). URL: <http://dx.doi.org/10.1002/2014EO200002>.
- [47] C. T. Russell. “Planetary magnetospheres”. In: *Reports on Progress in Physics* 56.6 (1993), p. 687. URL: <http://stacks.iop.org/0034-4885/56/i=6/a=001>.
- [48] C.T. Russell. “The dynamics of planetary magnetospheres”. In: *Planetary and Space Science* 49.10–11 (2001). Magnetosphere of the Outer Planets Part {II}, pp. 1005–1030. ISSN: 0032-0633. DOI: [http://dx.doi.org/10.1016/S0032-0633\(01\)00017-4](http://dx.doi.org/10.1016/S0032-0633(01)00017-4). URL: <http://www.sciencedirect.com/science/article/pii/S0032063301000174>.
- [49] F. Scholze, H. Rabus, and G. Ulm. “Mean energy required to produce an electron-hole pair in silicon for photons of energies between 50 and 1500 eV”. In: *Journal of Applied Physics* 84.5 (1998), pp. 2926–2939. DOI: [10.1063/1.368398](http://dx.doi.org/10.1063/1.368398). URL: <http://dx.doi.org/10.1063/1.368398>.
- [50] Angélica Sicard and Sébastien Bourdarie. “Physical Electron Belt Model from Jupiter’s surface to the orbit of Europa”. In: *Journal of Geophysical Research: Space Physics* 109.A2 (2004). A02216. ISSN: 2156-2202. DOI: [10.1029/2003JA010203](http://dx.doi.org/10.1029/2003JA010203). URL: <http://dx.doi.org/10.1029/2003JA010203>.
- [51] A. Sicard-Piet, S. Bourdarie, and N. Krupp. “JOSE: A New Jovian Specification Environment Model”. In: *IEEE Transactions on Nuclear Science* 58.3 (June 2011), pp. 923–931. ISSN: 0018-9499. DOI: [10.1109/TNS.2010.2097276](http://dx.doi.org/10.1109/TNS.2010.2097276).
- [52] Alan R. Smith et al. “Radiation events in astronomical CCD images”. In: vol. 4669. 2002, pp. 172–183. DOI: [10.1117/12.463423](http://dx.doi.org/10.1117/12.463423). URL: <http://dx.doi.org/10.1117/12.463423>.
- [53] M. de Soria-Santacruz et al. “An empirical model of the high-energy electron environment at Jupiter”. In: *Journal of Geophysical Research: Space Physics* 121.10 (2016). 2016JA023059, pp. 9732–9743. ISSN: 2169-9402. DOI: [10.1002/2016JA023059](http://dx.doi.org/10.1002/2016JA023059). URL: <http://dx.doi.org/10.1002/2016JA023059>.

- [54] M. de Soria-Santacruz Pich et al. "The GIRE2 model and its application to the Europa mission". In: *2016 IEEE Aerospace Conference*. Mar. 2016, pp. 1–7. DOI: 10.1109/AERO.2016.7500516.
- [55] *Stopping Powers for Electrons and Positrons*. Tech. rep. ICRU Report 37. International Commission on Radiation Units and Measurements, 1984.
- [56] D. J. Williams et al. "The Galileo Energetic Particles Detector". In: *Space Science Reviews* 60.1 (1992), pp. 385–412. ISSN: 1572-9672. DOI: 10.1007/BF00216863. URL: <http://dx.doi.org/10.1007/BF00216863>.
- [57] Gordon Wrenn. "Conclusive Evidence for Internal Dielectric Charging Anomalies on Geosynchronous Communications Spacecraft". In: *Journal of Spacecraft and Rockets* 32.3 (May 1995). doi:10.2514/3.26645, pp. 514–520.
- [58] A. Yamashita et al. "Radiation damage to charge coupled devices in the space environment". In: *IEEE Transactions on Nuclear Science* 44.3 (June 1997), pp. 847–853. ISSN: 0018-9499. DOI: 10.1109/23.603763.